crystals

MDPI

Review

Chiral 4f and 3d-4f Complexes from Enantiopure Salen-Type Schiff Base Ligands

Catherine P. Raptopoulou

Institute of Nanoscience and Nanotechnology, NCSR "Demokritos", 15310 Aghia Paraskevi Attikis, Greece; c.raptopoulou@inn.demokritos.gr; Tel.: +30-210-6503346

Abstract: This review summarizes the structural characteristics and physicochemical properties of chiral 4f and 3d-4f complexes based on enantiopure salen-type Schiff base ligands. The chirality originates from the enantiopure diamines and is imparted to the Schiff base ligands and complexes and finally to the crystal structures. The reported enantiopure Schiff base ligands derive from the condensation of aromatic aldehydes, such as salicylaldehyde and its various derivatives, and the enantiopure diamines, (1*R*,2*R*) or (1*S*,2*S*)-1,2-diamino-cyclohexane, (1*R*,2*R*) or (1*S*,2*S*)-1,2-diamino-1,2-diphenylethane, (*R*) or (*S*)-2,2′-diamino-1,1′-binaphthalene, and 1,2-diaminopropane.

Keywords: enantiopure Schiff base ligands; chiral metal complexes; lanthanide(III) complexes; chirality; Sohncke space groups

check for updates

Citation: Raptopoulou, C.P. Chiral 4f and 3d-4f Complexes from Enantiopure Salen-Type Schiff Base Ligands. *Crystals* **2024**, *14*, 474. https://doi.org/10.3390/cryst14050474

Academic Editor: Elizabeth A. Hillard

Received: 11 April 2024
Revised: 13 May 2024
Accepted: 16 May 2024
Published: 18 May 2024

1. Introduction

Molecular materials based on metal coordination complexes exhibit versatile electronic and structural features, which arise from the metal ions and the different types and numbers of ligands. These materials are usually prepared by wet chemistry methods, in some cases under environmentally friendly processes, and most importantly, combine different characteristics, such as metal oxidation states and versatile coordination geometries, with redox, catalytic, magnetic, electrical, and optical properties. The physicochemical properties of these materials depend on their exact structure and can be totally altered by small structural changes. Molecular materials with nonlinear optical, molecular magnetic, conducting, and superconducting properties have been proposed for potential applications [1,2]. Over the last decade, the field of molecular materials that combine different physical properties and are subjected to various external stimuli [3] has grown very rapidly. The rational design of these multifunctional molecular materials is of prime importance because of their potential applications in information storage, sensors, spintronics, biology, etc. [4].

Chirality is an intrinsic property of matter and is important in chemistry, biology, and physics, as it can affect the properties and reactivity of molecules. Chiral objects or molecules are not superimposable in their mirror image. The distinct left and right-handed forms are called enantiomers and exhibit different properties and activities. Eminent examples of chiral molecules are amino acids, sugars, and, therefore, proteins and nucleic acids, as well as certain pharmaceutical drugs. Metal coordination complexes can exhibit two types of chirality: (a) chirality at metal, which arises by the certain arrangement of ligands around the metal ion and disappears upon the separation of the metal and the ligands, and (b) chirality, which is imparted by the presence of chiral ligands around the metal ions [5]. Examples of metal complexes that belong in type (a) are the tetrahedral metal complexes with four different ligands, the octahedral tris-bidentate metal complexes, the octahedral bis-bidentate-bis-monodentate metal complexes, the octahedral metal complexes with three different monodentate ligands ($MA_2B_2C_2$), the octahedral metal complexes with four different ligands in the *fac*-arrangement ($MABCL_3$), and the octahedral metal complexes with linear tetradentate ligands in the *cis*-isomer (MD_4L_2). These chiral complexes

are referred to as chiral-at-metal or 'stereogenic-at-metal' complexes [6]. From the synthetic point of view, the use of enantiopure ligands for the enantioselective synthesis of chiral coordination complexes is the most efficient method [7].

Chiral metal complexes are important in modern medicine as potential therapeutics (metallodrugs) [8] and can be selectively activated at the target site of a biomolecule by an external stimulus. These compounds can act as 'prodrugs' that interact with the biomolecules via various mechanisms such as redox processes, metal coordination, photo- and thermal-activation, and radiation [9]. Besides their importance in the pharmaceutical industry, chiral metal complexes, which combine chirality with magnetic, optical, and electrical properties, have received great attention in recent years and constitute a new and fast-growing class of multifunctional molecular materials. Coordination complexes that combine chirality and single-molecule magnet behavior, and in addition, chirality-induced properties, e.g., ferroelectricity [10,11], second-order nonlinear optical properties [12,13], magnetochiral dichroism [14,15], magneto-optical Faraday effect [16,17], and circularly polarized luminescence [18,19], represent a special class of multifunctional molecular materials.

Lanthanide(III) ions display large spin ground states and magnetic anisotropy, therefore, have been widely used for the synthesis of homo- and hetero-metallic complexes which show single-molecule magnet (SMM) [20–22], and single-ion magnet (SIM) [23–28] behavior. Schiff bases are formed by the condensation reaction between a primary amine and an aldehyde or ketone. These compounds are widely used in organic synthesis and coordination chemistry as ligands for metal complexes. They are also important in the production of various pharmaceuticals, dyes, and pesticides, in the food and agrochemical industry, in catalysis and energy storage, and for environmental and biomedical applications [29–31]. Schiff base ligands can be easily synthesized by various combinations of carbonyl compounds and primary amines and can be easily functionalized by choosing starting materials with the desired side groups. The combination of chiral Schiff base ligands with lanthanide(III) ions has been an effective strategy for the development of multifunctional molecular materials. The present minireview summarizes the chiral 4f and 3d-4f coordination complexes with enantiopure Schiff base ligands derived from the condensation of aromatic aldehydes, such as salicylaldehyde and its various derivatives, and the enantiopure diamines, (1*R*,2*R*) or (1*S*,2*S*)-1,2-diamino-cyclohexane, (1*R*,2*R*) or (1*S*,2*S*)-1,2-diamino-1,2-diphenylethane, (*R*) or (*S*)-2,2′-diamino-1,1′-binaphthalene, and 1,2-diaminopropane. The complexes reported herein were published up to December 2023. The Schiff base ligands discussed herein are depicted in Schemes 1–3.

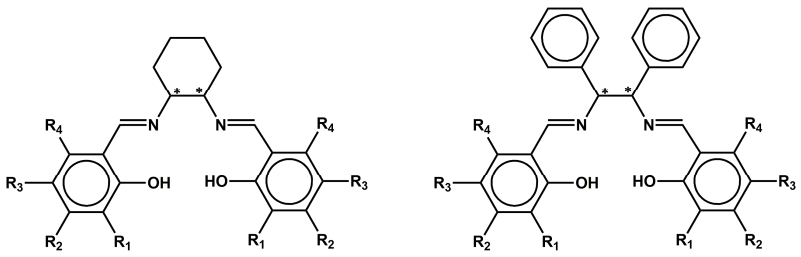

$R_1 = R_2 = R_3 = R_4 = H$, H_2L1
$R_1 = OMe$, $R_2 = R_3 = R_4 = H$, H_2L2
$R_1 = OEt$, $R_2 = R_3 = R_4 = H$, H_2L3
$R_1 = NO_2$, $R_2 = R_3 = R_4 = H$, H_2L4
$R_1 = R_2 = R_4 = H$, $R_3 = Cl$, H_2L5
$R_1 = R_2 = R_4 = H$, $R_3 = COOH$, H_2L6
$R_1 = R_3 = Cl$, $R_2 = R_4 = H$, H_2L7
$R_1 = CH_3$, $R_2 = R_3 = R_4 = H$, H_2L8

$R_1 = R_2 = R_3 = R_4 = H$, H_2L9
$R_1 = OMe$, $R_2 = R_3 = R_4 = H$, H_2L10
$R_1 = R_2 = OMe$, $R_3 = R_4 = H$, H_2L11

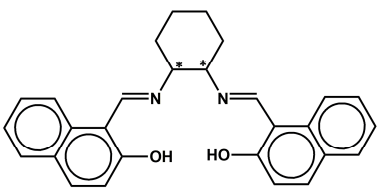

H_2L12

Scheme 1. The ligands H_2L1–H_2L12.

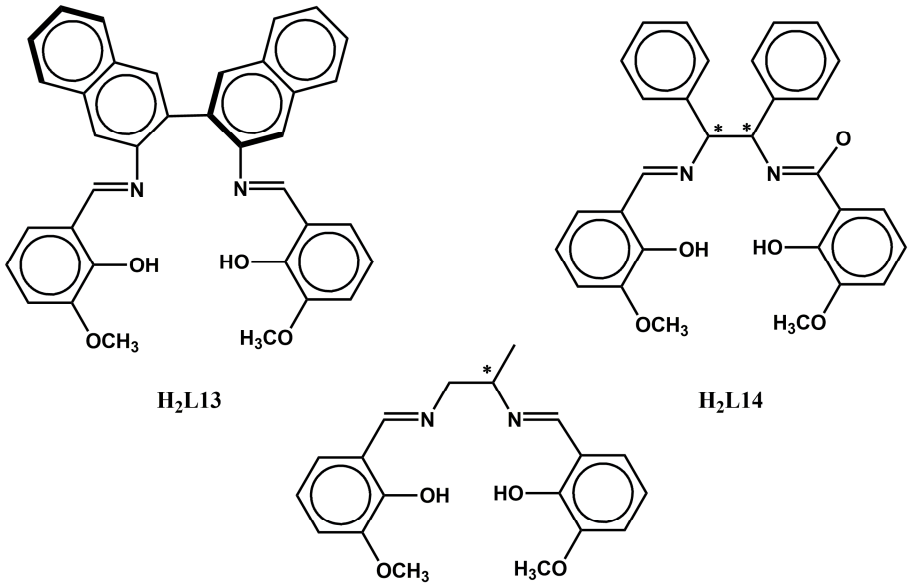

Scheme 2. The ligands H_2L13–H_2L15.

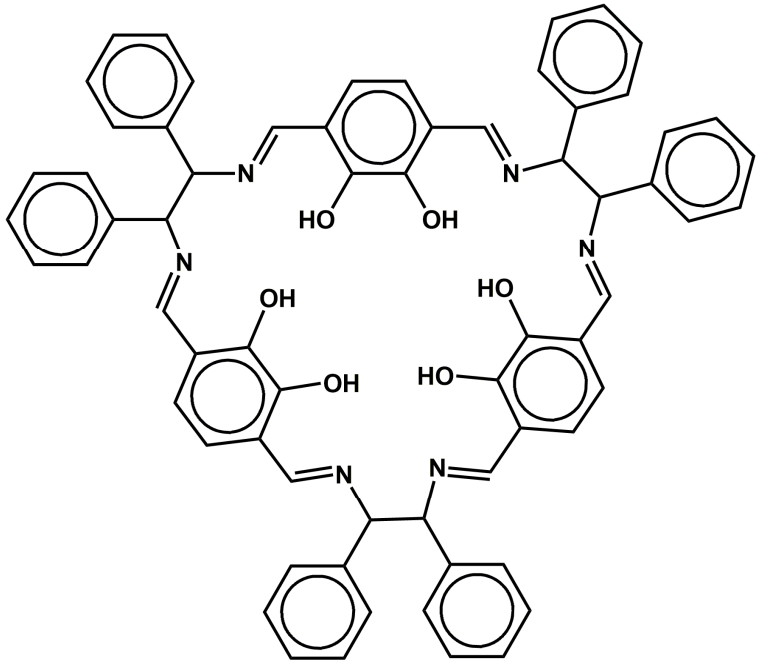

Scheme 3. The ligand H_2L16.

2. Homometallic 4f Complexes

Structural, CD, and magnetic data for the homometallic 4f complexes are listed in Table 1.

Table 1. Structural, CD, and magnetic data for the homometallic 4f complexes **1–10**.

Complex	4f Ion	Space Group	Coordination Number	CD, λ_{max} (nm)	$\chi_M T$ (r.t.) (cm^3Kmol^{-1})	U_{eff} (K)	t_0 (s)	Ref.
1*R*/1*S*	Dy	*C*2	8	-	14.40	39.90 [b]	3.62×10^{-6}	[32]
2*R*/2*S*	Dy	$P2_1$	7	-	13.84	13.27 [c]	2.02×10^{-6}	[33]
3*R*/3*S*	Tb	$P2_1$	7	−291, −391 +350 [a]	11.80	-	-	[33]
4*R*/4*S*	Ho	$P2_1$	7	-	14.12	-	-	[33]
5*R*	Ce	$P4_3$	8	−343, +320 [a]	-	-	-	[34]
6*R*	Dy	$P2_1$	8	-	-	-	-	[35]
7*S*	Er	$P2_1$	8	-	-	-	-	[36]
8*R*/8*S*	Dy	*C*2	7	−281, −389, +348 [a]	13.47	24.61 [c]	8.49×10^{-8}	[33]
9*S*	Sm	*C*2	10	-	-	-	-	[37]
10*R*	Ce	*P*1	9, 10	-	-	-	-	[38]

[a] the values correspond to the *R*-enantiomer, same values with opposite signs correspond to the *S*-enantiomer; [b] under 1.5 kOe external dc field; [c] under 2.0 kOe external dc field.

A pair of enantiopure complexes $(Et_3NH)[Dy^{III}(L4)_2]$ (**1*R*/1*S***) were reported which contain ligand $H_2L4_{RR,SS}$, *N*,*N*′-(1,2-cyclohexanediylethylene)bis(3-nitrosalicylideneiminato), Scheme 1 [32]. The asymmetric unit of complex **1*R*** contains two independent $[Dy^{III}(L4_{RR})_2]^-$ anions and four $(Et_3NH)^+$ cations. Each Dy^{III} ion is eight-coordinated to two $O_{phenoxo}$ and two N_{imino} atoms from two $(L4_{RR})^{2-}$ ligands with a triangular dodecahedron (TDD-8) geometry (CShM (Continuous Shape Measures) = 0.82632 (Dy1) and 1.14706 (Dy2)), Figure 1. The CD spectra of both **1*R*/1*S*** in the MeCN solution display mirror image patterns as expected for a pair of enantiomers. The magnetic properties of mononuclear complexes in which the Ln^{III} ion is encapsulated by two salen-type ligands are reported for the first time. Both complexes exhibit field-induced SIM behavior combined with chirality. Dual magnetic relaxations are observed under a weak DC field as a result of both single-ion anisotropy and a direct process due to intermolecular interactions. Under a higher dc field, a single thermally activated Orbach relaxation is observed due to single-ion anisotropy. Thus, a field-induced switch from dual relaxation to a single relaxation process is achieved.

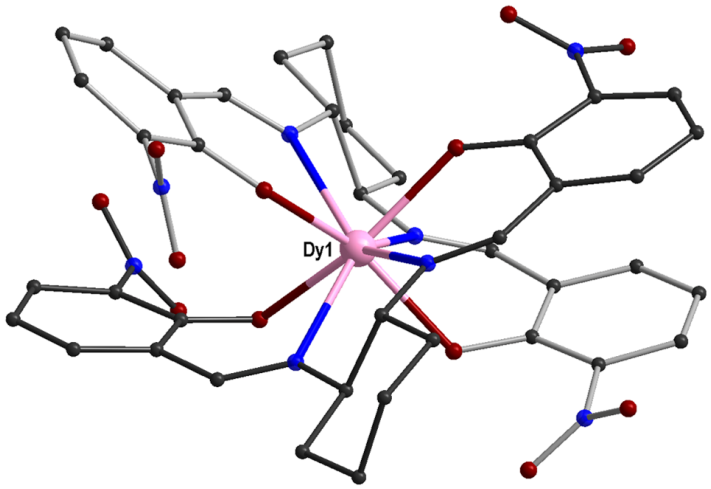

Figure 1. The molecular structure of one of the independent $[Dy^{III}(L4_{RR})_2]^-$ anions in **1*R***, CCDC-1424808 [32]. Color code: Dy pink, O red, N blue, C grey. The ligand in the front is shown with darker grey bonds for clarity purposes.

Pairs of enantiomerically pure chiral complexes with $H_2L5_{RR,SS}$ were reported with formula [(L_{OEt})Ln(L5)] (Ln^{III} = Dy (**2*R*/2*S***, Tb (**3*R*/3*S***), Ho (**4*R*/4*S***); L_{OEt} = [(Cp)Co(P(O)($OEt)_2)_3$]) which crystallize with two independent molecules in the asymmetric unit [33]. Both Ln^{III} ions are seven-coordinated to the two $O_{phenoxo}$ and two N_{imino} of $(L5)^{2-}$ and to three O-atoms from L_{OEt} in distorted monocapped triangular prism geometry. The enantiomeric nature of all complexes was confirmed by CD spectra. The temperature dependence of the magnetic susceptibility for **2*R*-4*R*** shows a gradual decrease of the $\chi_M T$ product in the range 300–100 K and a further sharp decrease at 2 K, which can be attributed to the progressive depopulation of the Stark levels and/or possible antiferromagnetic interactions between the metal ions. The magnetization of **2*R*-4*R*** at 2 K does not reach saturation at 70 kOe due to the ligand-field-induced splitting of the Stark levels and to the magnetic anisotropy. Complex **2*R*** shows field-induced slow relaxation of magnetization, which follows a thermally activated mechanism. The energy barrier and pre-exponential factor τ_0 (Table 1) were calculated by the Arrhenius law, $\tau = \tau_0 \exp\left(\frac{\Delta}{k_B T}\right)$. Complex **2*R*** represents a rare example of a seven-coordinated chiral SIM. Complexes **2*R*-4*R*** show second-order nonlinear optical (NLO) effects with responses of 0.3 times that of urea. Unfortunately, no ferroelectric properties were observed for **2*R*-4*R*** at room temperature.

The Ce^{IV} ion in complex [$Ce^{IV}(L7_{RR})_2$] (**5*R***) is eight-coordinated to the two $O_{phenoxo}$ and the two N_{imino} atoms from two $(L7_{RR})^{2-}$ ligands in distorted square antiprism geometry [34]. The dihedral angle between the best mean planes of the two ligands, excluding the C-atoms of the cyclohexane ring, is 47.1°, and this is a unique architecture for Ce^{IV} complexes with two Schiff base ligands (Figure 2). The Ce-O and Ce-N bond distances are 2.212(5)-2.241(5) Å and 2.550(7)-2.570(6) Å, respectively. The complex was studied by CD, ^{1}H NMR, ^{13}C NMR, and NOE (nuclear Overhauser effect) studies; the latter showed that the azomethine H-atom is in proximity to the phenyl ring H-atom and the cyclohexane CH_2. The spectral analysis suggests Ce^{IV} ion in a distorted planarity of the N_2O_2 chromophore group.

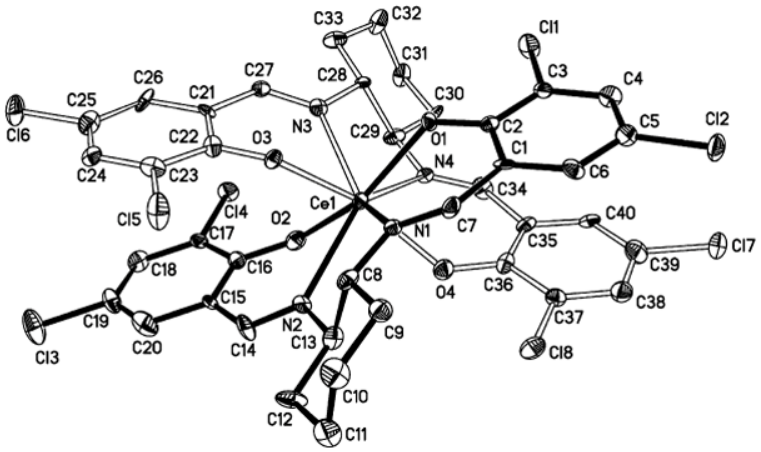

Figure 2. The labeled molecular structure of **5*R***. The ligands are displayed with filled and open bonds to visualize their spatial arrangement around the central ion (C1-C20 and C21-C40, respectively) [34]. Copyright © 2008 Elsevier Ltd. All rights reserved.

The same ligand gave complex (cation)[$Dy^{III}(L7_{RR})_2$] (**6*R***) [35]. The Dy^{III} ion is eight-coordinated to two $O_{phenoxo}$ and two N_{imino} atoms from two $(L7_{RR})^{2-}$ ligands and displays square antiprism geometry with Δ absolute configuration. The countercation was formed in situ from the decomposition of H_2L7_{RR} with $Dy(NO_3)_3$ acting as a Lewis acid catalyst. Single crystal samples of **6*R*** at r.t. show ferroelectric behavior with remnant polarization P_r~4.51 μCcm^{-2} and E_c~28.11 kVcm^{-1} and characteristic emission $^4F_{9/2} \rightarrow {}^6H_{15/2}$ and $^4F_{9/2} \rightarrow {}^6H_{13/2}$ transitions of Dy^{III} at the solid luminescent spectrum (Figure 3). The enantiopure ligand H_2L7_{SS} (Scheme 1) gave complex (cation)[$Er^{III}(L7_{SS})_2$] (**7*S***), which

is isomorphous to complex **6*R***, but in enantiomeric configuration [36]. The Er^{III} ion shows an eight-coordinate square antiprism geometry with Λ absolute configuration due to the *S*,*S*-enantiomer of the diamine used. Single crystal samples of **7*S*** at r.t. show ferroelectric behavior with remnant polarization P_r~7.98 μCcm^{-2} and E_c~22.12 kVcm^{-1} at electric field 24 kVcm^{-1}. The value of P_r is close to that of P_s~8.04 μCcm^{-2}, which is much larger than that of other ferroelectrics, such as KH_2PO_4, triglycine sulfate, and $NaKC_4H_4O_6{\cdot}4H_2O$. Both H_2L7_{SS} and **7*S*** show second harmonic generation (SHG) efficiency, 0.6 and 1.2 times that of urea, respectively, thus confirming their potential as second-order NLO materials.

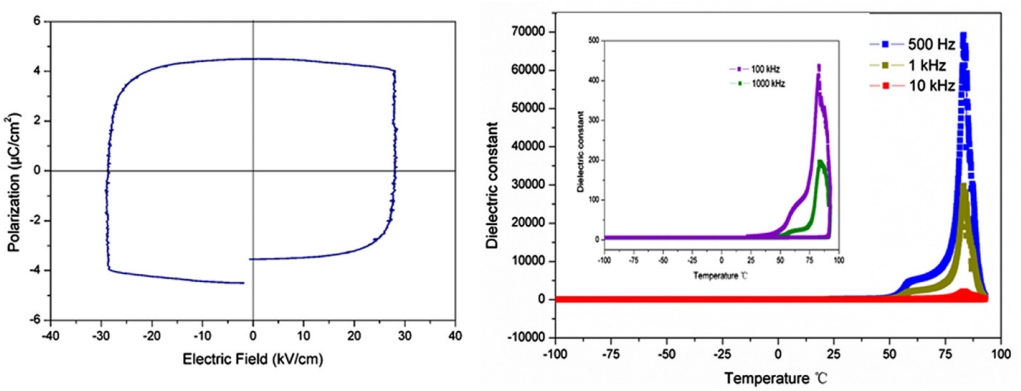

(**a**) (**b**)

Figure 3. (**a**) Electric hysteresis loop of **6*R*** at r.t. for single crystal sample. (**b**) Temperature dependence of the dielectric constant of **6*R*** at various frequencies. Inset: dielectric constant at high frequencies [35]. Copyright © 2014 Elsevier B.V. All rights reserved.

A pair of enantiopure complexes, namely [(L_{OEt})Dy(L9)] (**8*R*/8*S***) was also reported (L_{OEt} = [(Cp)Co(P(O)(OEt)$_2$)$_3$]) [33]. In both complexes, the Dy^{III} ions are seven-coordinated to the $(O_{phenoxo}N_{imino})_2$ donor set of $(L9)^{2-}$ and to three O-atoms from L_{OEt} ligand, with distorted monocapped triangular prism geometry (Figure 4). The CD spectra of **8*R*/8*S*** in KBr pellets confirm the enantiomeric nature of both compounds (Figure 5, Table 1). The complex exhibits field-induced SIM behavior. The relaxation follows a thermally activated mechanism (Table 1). Complex **8*R*** is similar to complex **2*R*-4*R*** and displays similar second-order NLO effects, with no ferroelectric behavior at r.t.

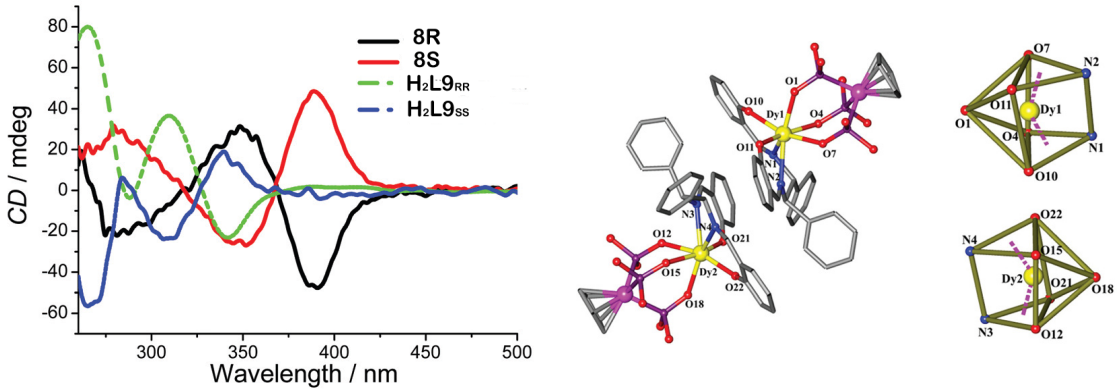

(**a**) (**b**)

Figure 4. (**a**) CD spectra of **8*R*/8*S*** and $H_2L9_{RR,SS}$ in KBr pellets. (**b**) Partially labeled plot of the molecular structure of **8*R*** and local coordination geometry of the Dy^{III} ions; ethyl groups of the phosphates and H-atoms are omitted for clarity. Reproduced from Ref. [33] with permission from the Royal Society of Chemistry.

The zwitterion of enantiopure ligand H_2L10_{SS} (Scheme 1) gave complex $[Sm^{III}(H_2L10_{SS})(NO_3)_3]$ (**9*S***), which crystallizes with two independent molecules in the asymmetric unit [37]. The Sm^{III} ion is ten-coordinated to three chelate nitrato groups and to the two $O_{phenoxo}$ and two $O_{methoxo}$ atoms of the zwitterion H_2L10_{SS}. Both N_{imino} atoms are protonated and form intramolecular N-H···$O_{phenoxo}$ hydrogen bonds. Hirshfeld surface analysis shows that the crystal packing is dominated by H···H, O···H and C···H contacts.

The enantiopure ligand H_2L12_{RR} (Scheme 1) gave the chiral 2D coordination polymer $[Ce^{III}_2(H_2L12_{RR})_6(NO_3)_6(H_2O)]_n$ (**10*R***) [38]. Ce(2) is nine-coordinated to three chelate nitrato groups and three $O_{phenoxo}$ from three different H_2L12_{RR} ligands. Ce(1) is ten-coordinated, exhibiting the same coordination environment as Ce(2) and also an additional water molecule. Complex **10*R*** shows 2D square grid network architecture. Both H_2L12_{RR} and complex **10*R*** were tested on MDA-MB-231 breast cancer cells by MTT assay and showed antiproliferative activity, which is higher for complex **10*R*** compared with H_2L12_{RR}.

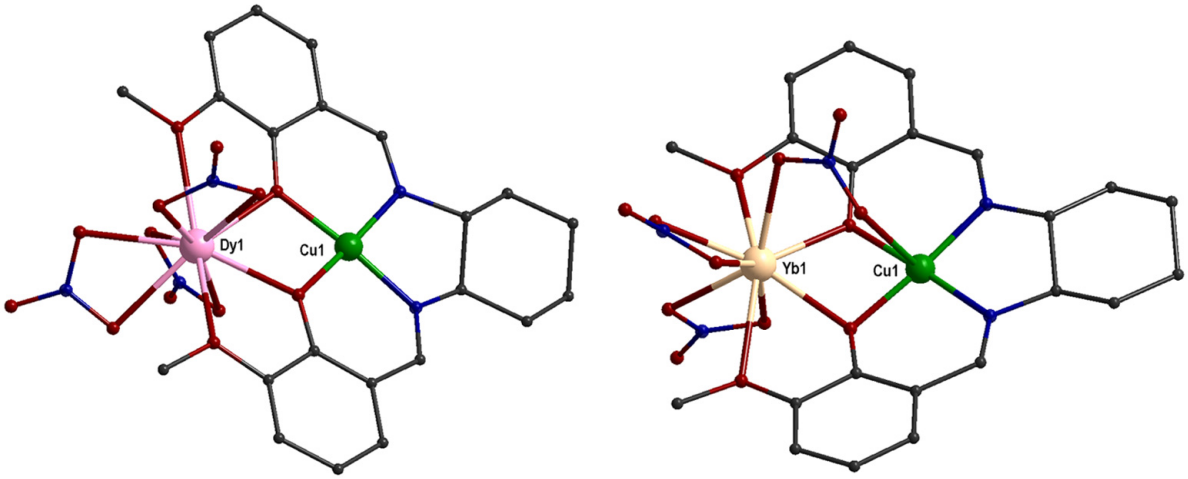

Figure 5. The molecular structure of one of the independent molecules in **17*R*** (CCDC-1046379, **left**) and **20*R*** (CCDC-1046384, **right**) [39]. Color code: Dy pink, Yb tan, O red, N blue, C grey.

3. Heterometallic 3d-4f Complexes

The structural, CD, and magnetic data for the heterometallic 3d-4f complexes are summarized in Tables 2–4. Other spectroscopic data are listed in Table 5.

The enantiopure ligand H_2L2_{RR} (Scheme 1) gave a family of CuLn dinuclear complexes, $[CuLn(L2_{RR})(NO_3)_3(H_2O)]$ (Ln^{III} = Ce (**11*R***), Nd (**12*R***)), and $[CuLn(L2_{RR})(NO_3)_3]$ (Ln = Sm (**13*R***), Eu (**14*R***), Gd (**15*R***), Tb (**16*R***), Dy (**17*R***), Ho (**18*R***), Er (**19*R***) and Yb (**20*R***)), which crystallize with two independent dimers in the asymmetric unit (Figure 5) [39]. Temperature-controlled reversible conversion of one chiral crystal (**15*R*-17*R***) to another chiral crystal (**15′*R*-17′*R***) was observed, which leads to polymorphism and space group transformation from *P*1 to $P2_1$. The metal ions are linked through two $O_{phenoxo}$ bridges. The Cu^{II} ion in **11*R*-17*R*** is coordinated to the two $O_{phenoxo}$ and the two N_{imino} atoms of $(L2_{RR})^{2-}$ in a square planar geometry, whereas in **15′*R*-17′*R*** and **18*R*-20*R*** a weak bond to one $O_{nitrato}$ leads to square pyramidal geometry. The Ln^{III} ion in **13*R*-17*R*** is ten-coordinated to two bridging $O_{phenoxo}$, two $O_{methoxo}$, and three chelate nitrato groups, whereas, in **11*R*** and **12*R*,** the Ln^{III} ion is eleven-coordinated due to an additional coordinated water molecule. In **15′*R*-17′*R*** and **18*R*-20*R***, one Ln^{III} ion is ten-coordinated as in **13*R*-17*R***, and the second Ln^{III} ion is nine-coordinated because one of the nitrato groups is monodentate. The Cu···Ln distances are in the range 3.2287(7)-3.4382(13) Å in going from **20*R*** to **11*R***. The CD spectra of the aforementioned complexes confirmed their optical activity and enantiomeric nature. Complexes **15*R*-17*R*** and **15′*R*-17′*R*** show ferromagnetic coupling between the metal ions. The Tb^{III}, Dy^{III}, and Ho^{III} compounds, **16*R*/16′*R*, 17*R*/17′*R***, and **18*R*** display field-induced magnetic relaxation phenomena (Table 3). The magnetic difference between

these complexes results from the lanthanide contraction effect of the Ln^{III} ions. Complex **15′*R*** and [CuLu($L2_{RR}$)$(NO_3)_3$] (**21*R***) were previously reported [40].

Complexes [NiLn($L2_{RR}$)$(NO_3)_3(H_2O)$] (Ln = Ce (**22*R***), Nd (**23*R***)) and [NiLn($L2_{RR}$)$(NO_3)_3$] (Ln = Nd (**24*R***), Sm (**25*R***), Eu (**26*R***), Gd (**27*R***), Tb (**28*R***), Dy (**29*R***), Yb (**30*R***), and Lu (**31*R***)) are isomorphous to abovementioned complexes **11*R*-14*R***, **15′*R*-17′*R***, **20*R*** and **21*R*** [40–42]. Complexes **28*R*** and **29*R*** exhibit field-induced SMM behavior due to the strong anisotropy and crystal field effect of the Tb^{III} or Dy^{III} ions (Figure 6, Table 2).

Complex [ZnLu($L2_{RR}$)$(NO_3)_2(CH_3CO_2)$] (**32*R***) consists of a five-coordinate Zn^{II} ion with square pyramidal geometry defined by the two $O_{phenoxo}$ and the two N_{imino} atoms of the ligand and one O-atom from the μ_2-$CH_3CO_2^-$, and a nine-coordinate Lu^{III} ion bound to two bridging $O_{phenoxo}$, two $O_{methoxo}$, two chelate nitrato groups and one O-atom from the μ_2-$CH_3CO_2^-$ [40]. The enantiomeric nature of all the abovementioned complexes was confirmed by solid-state CD spectroscopy.

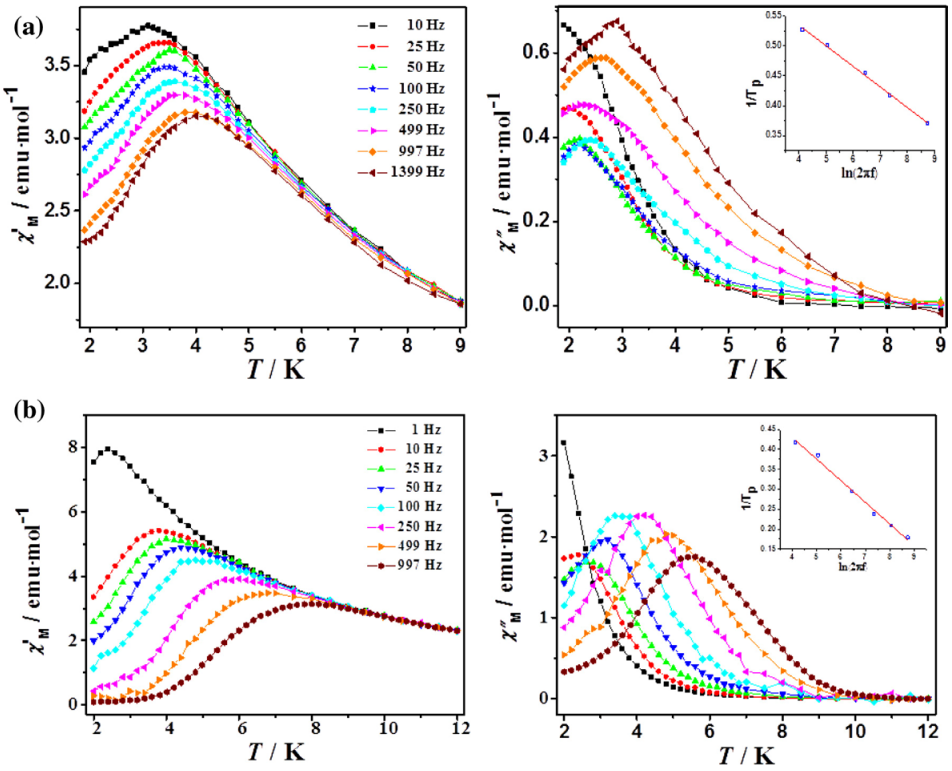

Figure 6. Temperature dependence of the χ_{ac} at different frequencies with H_{dc} = 2 kOe and H_{ac} = 2.5 kOe and the least-squares fit of the experimental data to the Arrhenius equation for **28*R*** (**a**) and **29*R*** (**b**) [41]. Copyright © 2015 Elsevier B.V. All rights reserved.

A pair of enantiomer tetranuclear complexes [Cu_2Tb_2(L2)$(N_3)_6(MeOH)_2$] (**33*R*/33*S***) crystallize with one cluster in the asymmetric unit (Figure 7) [43]. The CuTb subunits are related to each other through a pseudo inversion center and are bridged by two end-on azides. The two Cu^{II} ions are octahedral and coordinated to the two $O_{phenoxo}$ and the two N_{imino} atoms of $(L2)^{2-}$, one $\mu_{1,3}$-N_3^-, and one MeOH. The two Tb^{III} ions are eight-coordinated to the two bridging $O_{phenoxo}$ and the two $O_{methoxo}$ of $(L2)^{2-}$, one $\mu_{1,3}$-N_3^-, one terminal N_3^- and two $\mu_{1,1}$-N_3^- in bicapped trigonal prism geometry. The ac susceptibility studies under zero dc field showed slow relaxation of magnetization (Table 3). The SMM behavior was confirmed by the hysteresis loops observed on field-oriented single crystals of **33*R*** below 4 K (Figure 8). This is the first time that angular resolved magnetometry measurements and ab initio calculations were performed on polynuclear SMMs in order to determine the magnetic anisotropy axis of each individual Tb^{III} ion.

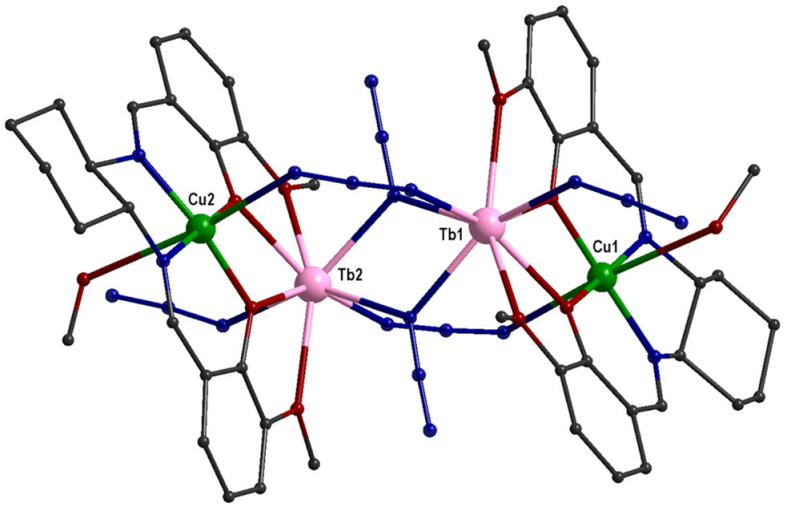

Figure 7. The molecular structure of **33*R***, CCDC-1000153, [43]. Color code: Tb pink, Cu green, O red, N blue, C grey.

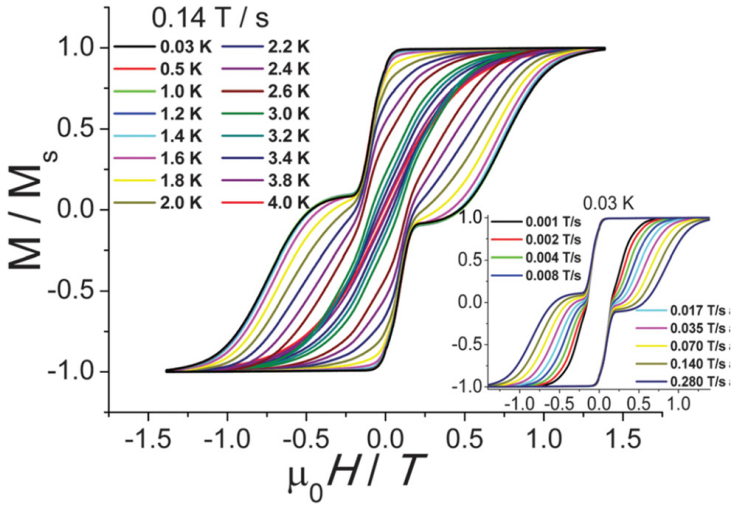

Figure 8. The hysteresis loops of **33*R*** measured on a single crystal on a μ-SQUID at the indicated temperatures and field sweep rates. Reproduced from Ref. [43] with permission from the Royal Society of Chemistry.

A family of Zn_2Dy chiral SIMs were reported by using enantiopure H_2L2_{RR} and H_2L2_{SS} ligands, complexes $[Zn_2Dy(L2_{RR})_2(X)_2(H_2O)](anion)$ (X = Cl^-, anion = ClO_4^- (**34*R***); X = Cl^-, anion = $CF_3SO_3^-$ (**35*R***); X = Br^-, anion = $CF_3SO_3^-$ (**36*R***)) and $[Zn_2Dy(L2_{SS})_2(X)_2(H_2O)]$ $[Zn_2Dy(L2_{SS})_2(X)_2(MeOH)](anion)_2$ (X = Cl^-, anion = ClO_4^- (**37*S***); X = Cl^-, anion = $CF_3SO_3^-$ (**38*S***); X = Br^-, anion = $CF_3SO_3^-$ (**39*S***)) [44]. All complexes are isomorphous. The asymmetric unit of **34*R*-36*R*** contains two independent molecules, whereas, in **37*S*-39*S***, the two molecules differ in the coordinated solvent molecule. Each Zn^{II} ion is five-coordinated to the two $O_{phenoxo}$ and the two N_{imino} atoms of $(L2)^{2-}$ and to the X^- ligand, which occupies the apex of the square pyramid. Each Dy^{III} ion is nine-coordinated to the two bridging $O_{phenoxo}$ and the two $O_{methoxo}$ atoms of each $(L2)^{2-}$ and one solvent molecule in muffin (MFF-9) geometry (Dy1, Dy2 (**34*R***, **37*S***), Dy1 (**35*R***, **36*R***, **38*S***, **39*S***)) and spherical tricapped trigonal prism, TTP-9 (Dy2 (**35*R***, **36*R***, **38*S***, **39*S***)). The molecular structure of complex **34*R*** is given in Figure 9. Solid-state CD spectra of all complexes confirmed their chiral nature and optical activity (Table 4). Both the coordinated anions and the counterions, as well as the coordinated solvent molecules, have important effects on the SIM behavior and on the second-harmonic generation and third-harmonic generation NLO properties of the

chiral complexes (Table 5). All complexes display field-induced magnetic relaxation as indicated by the peaks in the χ'' vs. T curves. The data in the lnτ vs. 1/T plots are not linear, which suggests that the relaxation has an Orbach process in addition to the Raman process. The curves were fitted with the equation $\tau^{-1} = CT^n + \tau_0^{-1}\exp\left(-\frac{U_{eff}}{kT}\right)$ to consider both processes and give the values listed in Table 4. Theoretical calculation further confirmed the experimental data. The study of the NLO properties showed that the SHG signal intensity of the **37*S*-39*S*** complexes is much stronger than that of the **34*R*-36*R*** because of the MeOH coordination in the former (Figure 10). Moreover, the bromide coordination and the perchlorate counteranion favor the SHG properties between the **37*S*-39*S*** complexes. The third harmonic generation (THG) signal intensity of the **34*R*-36*R*** complexes is much stronger than that of the **37*S*-39*S*,** which suggests that the coordination of the H_2O molecule favors the THG properties. Moreover, the triflate counteranion favors the THG properties between the **34*R*-36*R*** complexes.

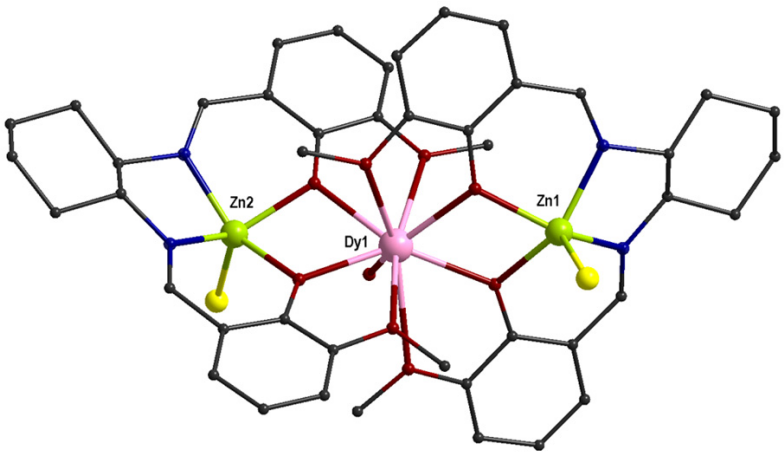

Figure 9. The molecular structure of one of the independent molecules in **34*R***, CCDC-2182147, [44]. Color code: Dy pink, Zn lime, Cl yellow, O red, N blue, C grey.

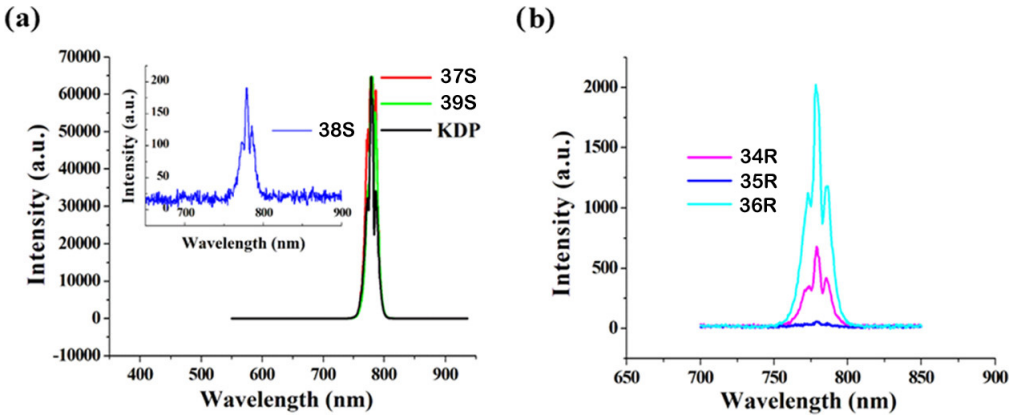

Figure 10. SHG spectra of crystalline samples of **37*S*-39*S*** (**a**) and **34*R*-36*R*** (**b**) with KH_2PO_4 (KDP) under excitation at λ = 1550 nm (T_{int} = 0.5 s). Reprinted with permission from Inorg. Chem. 2022, 61, 18510–18523 [44]. Copyright © 2022, American Chemical Society.

Enantiopure ligands H_2L2_{RR} and H_2L2_{SS} gave a family of 3d-3d′-4f chiral complexes, $[(Tp^*)Fe(CN)_3Cu(L2)Ln(NO_3)_3(H_2O)_3][(Tp^*)Fe(CN)_3]$ (Ln^{III} = Gd (**40*R*/40*S***), Tb (**41*R*/41*S***), Dy (**42*R*/42*S***); Tp* = hydridotris(3,5-dimethylpyrazol-1-yl)borate) which are isomorphous (Figure 11, Table 3) [45]. The Fe^{III} ions are six-coordinated to the three C-atoms from CN^- and the three N-atoms from pyrazolyl groups in a distorted octahedral geometry. The Cu^{II} ions are five-coordinated to the two $O_{phenoxo}$ and the two N_{imino} atoms of $(L2)^{2-}$ and the

bridging cyanide group in the apex of a square pyramid. The Ln^{III} ions are nine-coordinated to the two bridging $O_{phenoxo}$ and the two $O_{methoxo}$ of $(L2)^{2-}$, one chelate nitrate, and three aqua ligands in a geometry between spherical capped square antiprism (CSAPR-9) and capped square antiprism J10 (JCSAPR-9). CD spectra confirm the enantiomeric nature of the complexes. Magnetic studies revealed ferromagnetic interactions between the metal ions without signs of SMM behavior under zero or 1 kOe dc field. This indicates fast QTM relaxation as a result of the observed distorted coordination symmetry, which disfavors the axial anisotropy of the Tb^{III} and Dy^{III} ions.

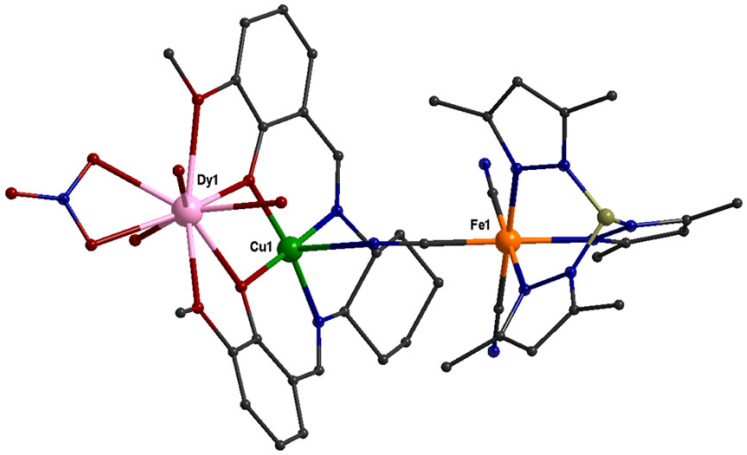

Figure 11. The molecular structure of the cation in **42*R***, CCDC-1537066, [45]. Color code: Dy pink, Cu green, Fe orange, B light grey, O red, N blue, C dark grey.

The enantiopure ligand H_2L3_{RR} (Scheme 1) gave the chiral complex $[CuEu(L3_{RR})(NO_3)_3]$ (**43*R***), which crystallizes with two independent molecules in the asymmetric unit (Table 3). The Cu^{II} ion is square planar, bound to the $(O_{phenoxo}N_{imino})_2$ donor set of $(L3_{RR})^{2-}$, and the Eu^{III} is ten-coordinated bound to the $(O_{phenoxo}O_{ethoxo})_2$ donor set of $(L3_{RR})^{2-}$ and to three chelate nitrato groups [46]. The chiral 1D zigzag chains of $[CuGd(L3)(NO_3)_3]_n$ (**44*R*/44*S***) were also reported (Table 3). The polymer structure is promoted by the semi-coordination of nitrate to Cu^{II}. Magnetic studies showed strong ferromagnetic coupling between the metal ions [47].

The enantiopure ligand H_2L6_{RR} (Scheme 1) was synthesized by the condensation reaction of 4-formyl-3-hydroxybenzoic acid and (1*R*,2*R*)-(-)-1,2-diaminocyclohexane. The ligand gave four chiral 1D coordination polymers, $[Mn_2Ln_2(L6_{RR})_2Cl_2(NO_3)_2(dmf)_6(H_2O)_2]_n$ (Ln^{III} = Pr (**45*R***), Nd (**46*R***), Sm (**47*R***), Gd (**48*R***)), (Table 2) [48]. The Mn^{III} ion is coordinated to the two $O_{phenoxo}$ and the two N_{imino} of $(L6_{RR})^{2-}$, one chlorido, and one monodentate nitrato group in a distorted octahedral geometry. Each carboxylato group of $(L6_{RR})^{2-}$ links two Ln^{III} ions in μ_2-fashion, thus forming a distorted square paddle-wheel unit $Ln^{III}{}_2$. Each Ln^{III} ion is eight-coordinated to four $O_{carboxylato}$, three dmf, and one H_2O molecules (Figure 12). The activity of **45*R*-48*R*** as heterogeneous enantioselective catalysts for the sulfoxidation reaction of various alkyl and aryl sulfides revealed that **45*R*-47*R*** show comparable activity for the oxidation of methyl *p*-tolylsulfide, whereas **48*R*** displays maximum conversion of 100% methyl phenylsulfoxide with 88% selectivity after 16 h and could be reused three times without loss of activity.

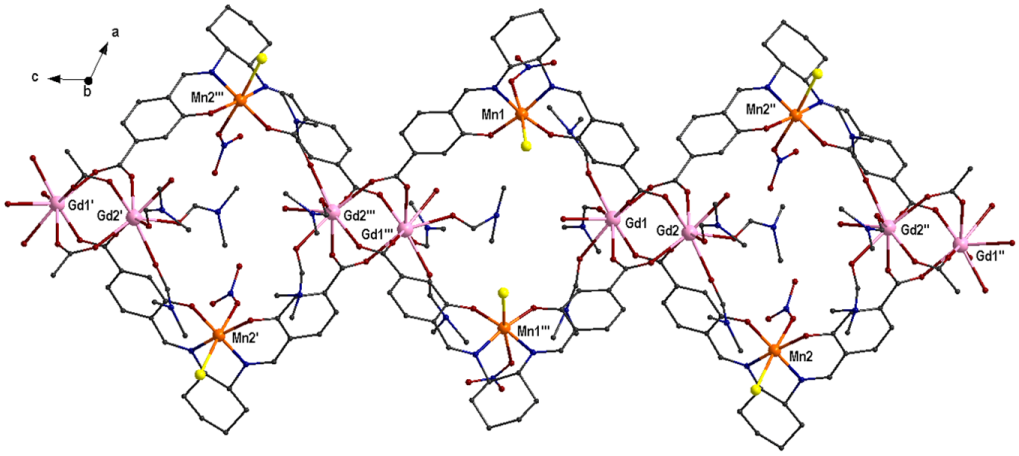

Figure 12. Part of the chiral 1D chain of **48*R***, CCDC-1471181, [48]. Color code: Gd pink, Mn orange, Cl yellow, O red, N blue, C grey. Symmetry operations: (′) $x, y, 1 + z$; (″) $2 - x, y, 1 - z$; (‴) $2 - x, y, 2 - z$.

The enantiopure ligands H_2L8_{RR} and H_2L8_{SS} (Scheme 1) gave pairs of chiral complexes [ZnLn(L8)(N(SiHMe$_2$)$_2$)(AABP)] (Ln^{III} = Y (**49*R*/49*S***), Lu (**50*R*/50*S***), Dy (**51*R*/51*S***), Sm (**52*R*/52*S***), La (**53*R*/53*S***); AABP = alkoxy-amino-bis(phenolato)), (Table 4) [49]. The Zn^{II} ion is five-coordinate to the two $O_{phenoxo}$ and the two N_{imino} atoms of $(L8)^{2-}$ and to the nitrogen of N(SiHMe$_2$)$_2$ in distorted square pyramidal geometry. The Ln^{III} ion is six-coordinated to the two bridging $O_{phenoxo}$ atoms of $(L8)^{2-}$ and to the three O- and the N-atoms of AABP in distorted octahedral geometry (Figure 13). Complexes **51*R*/51*S*** and **52*R*/52*S*** are highly efficient catalysts for copolymerization of CO_2 with cyclohexene oxide. The transformation of CO_2 to other chemicals is very important, both economically and environmentally, and can be achieved via the ring-opening copolymerization of CO_2 with epoxide to produce polycarbonates. The reaction requires selectivity in order to avoid other byproducts. It was shown that the ionic radii of the lanthanide ions influence the carbonate linkage, thus leading to excellent selectivity for the isolation of polymers only.

Table 2. Structural, CD, and magnetic data for the heterometallic Mn/4f and Ni/4f complexes.

Complex	3d/4f Ions	Space Group	Coordination Number	CD, λ_{max} (nm)	$\chi_M T$ (r.t.) (cm^3Kmol^{-1})	U_{eff} (K)	t_0 (s)	Ref.
22*R*	Ni/Ce	*P*1	11	−280, −400 +558 [a]	0.86	-	-	[41]
23*R*	Ni/Nd	*P*1	11	−280, −400 +558 [a]	2.36	-	-	[41]
24*R*	Ni/Nd	*P*1	10	-	-	-	-	[42]
25*R*	Ni/Sm	*P*1	10	−280, −400 +558 [a]	0.18	-	-	[41]
26*R*	Ni/Eu	*P*1	10	−280, −400 +558 [a]	1.05	-	-	[41]
27*R*	Ni/Gd	*P*1	10	−280, −400 +558 [a]	8.12	-	-	[41]
28*R*	Ni/Tb	*P*1	10	−280, −400 +558 [a]	12.26	29.12 [b]	3.21×10^{-9}	[41]
29*R*	Ni/Dy	*P*1	10	−280, −400 +558 [a]	14.87	18.40 [b]	7.39×10^{-6}	[41]
30*R*	Ni/Yb	*P*1	10	−280, −400 +558 [a]	1.46	-	-	[41]
31*R*	Ni/Lu	*P*1	10	-	-	-	-	[40]
54*R*	Ni/Ce	*C*2	10	-	-	8.5 [c]	7.7×10^{-5}	[50]
55*R*	Ni/Nd	*C*2	10	-	-	9.2 [b]	1.9×10^{-5}	[50]

Table 2. *Cont.*

Complex	3d/4f Ions	Space Group	Coordination Number	CD, λ_{max} (nm)	$\chi_M T$ (r.t.) (cm^3Kmol^{-1})	U_{eff} (K)	t_0 (s)	Ref.
56*R*/56*S*	Ni/Eu	*C*2	10	−325, +290, +370, +410 [a]	-	-	-	[50]
57*R*	Ni/Dy	*C*2	10	-	-	9.3 [b]	2.1×10^{-5}	[50]
58*R*	Ni/Er	*C*2	10	-	-	18.4 [b]	1.7×10^{-6}	[50]
59*S*	Ni/Yb	*C*2	10	-	-	18.1 [b]	2.1×10^{-6}	[50]
45*R*	Mn/Pr	*C*2	8	-	-	-	-	[48]
46*R*	Mn/Nd	*C*2	8	-	-	-	-	[48]
47*R*	Mn/Sm	*C*2	8	-	-	-	-	[48]
48*R*	Mn/Gd	*C*2	8	-	-	-	-	[48]

[a] the values correspond to the *R*-enantiomer, same values with opposite signs correspond to the *S*-enantiomer; [b] under 1.0 kOe external dc field; [c] under 0.5 kOe external dc field.

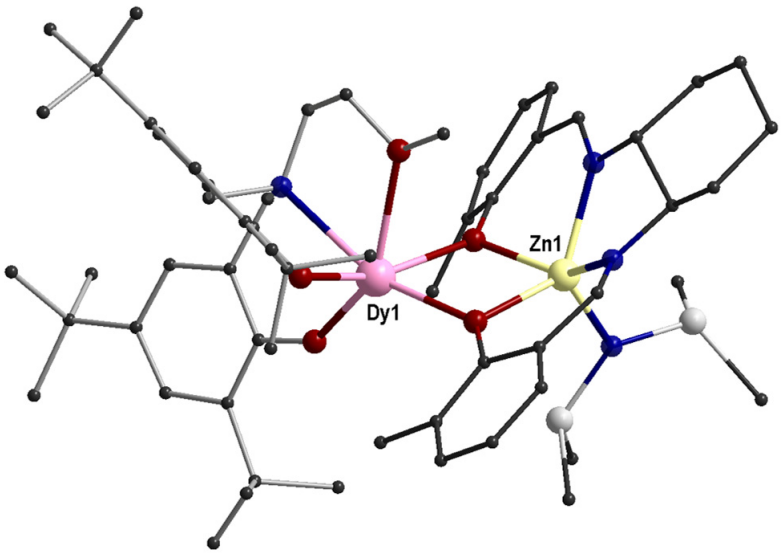

Figure 13. The molecular structure of the cation in **51*R***, CCDC-1870215, [49]. Color code: Dy pink, Zn yellow, Si light grey, O red, N blue, C dark grey.

The pair of enantiomers, ligands H_2L10_{RR} and H_2L10_{SS} (Scheme 1), gave the chiral complexes [NiLn(L10)$(NO_3)_3$] (Ln^{III} = Ce (**54*R***), Nd (**55*R***), Eu (**56*R*/56*S***), Dy (**57*R***), Er (**58*R***), Yb (**59*S***)) and [ZnLn(L10)$(NO_3)_3$(MeOH)] (Ln^{III} = Ce (**60*R***), Nd (**61*R***), Eu (**62*R*/62*S***), Dy (**63*S***), Er (**64*S***), Yb (**65*S***)) [50]. Both complexes **56*R*** and **56*S*** crystallize with two independent molecules in the asymmetric unit (Table 2). The Ni^{II} ion is bound to the two $O_{phenoxo}$ and the two N_{imino} atoms of $(L10)^{2-}$ in a square planar geometry, and the Eu^{III} ion is ten-coordinated to the two bridging $O_{phenoxo}$ and the two $O_{methoxo}$ of $(L10)^{2-}$ and to three bidentate nitrato groups with sphenocorona geometry (CShM = 3.24). Complexes **62*R*** and **62*S*** crystallize with two independent molecules in the asymmetric unit (Table 4). Complexes **62*R*/62*S*** are similar to **56*R*/56*S***, with the only difference being that the Zn^{II} ion in the former is bound to a MeOH molecule in the apex of a square pyramid. The solution CD spectra of the enantiomer pairs display mirror image patterns as expected (Figure 14). Complexes **54*R***, **55*R***, **59*S***, **60*R***, and **61*R***, i.e., complexes with Ln^{III} = Ce, Nd, and Yb, show slow relaxation of magnetization under an externally applied dc field, which is applied in order to avoid quantum tunneling of magnetization (QTM), and represent scarce examples of molecules with SIM behavior from 'uncommon magnetic lanthanides'. The fitting of the data by using the generalized Debye model according to the equation $\ln\left(\frac{\chi''_M}{\chi'_M}\right) = \ln(\omega\tau_0) - U_{eff}/(k_BT)$ gave the values listed in Tables 2 and 4. Additionally,

complexes with Ln^{III} = Dy and Er, i.e., **57*R***, **58*R*** and **63*S*** show field-induced SIM behavior, whereas ZnEr complex **64*S*** does not show signs of slow relaxation of the magnetization. The U_{eff} (τ_0) values for **57*R*** were calculated according to the generalized Debye model (Table 2). For **58*R*** and **63*S***, the data were fitted according to the Arrhenius equation $\ln\left(\frac{1}{2\pi\omega}\right) = \ln\left(\frac{1}{\tau_0}\right) - U_{eff}/(k_BT)$, which gave the values listed in Tables 2 and 4, respectively.

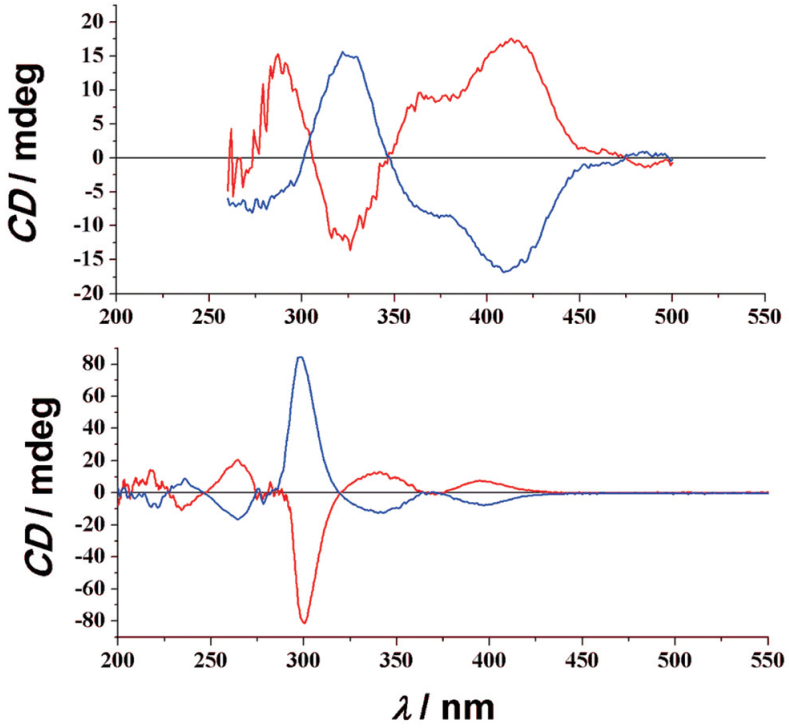

Figure 14. Solution CD spectra for the **56*R*/56*S*** (**top**) and **62*R*/62*S*** (**bottom**) pairs of enantiomers. R-enantiomers, red lines; S-enantiomers, blue lines. Reproduced from Ref. [50] with permission from the Royal Society of Chemistry.

The pair of enantiomers [ZnDy(L10)$(NO_3)_3(H_2O)$] **66*R*/66*S*** are isomorphous and crystallize with two independent molecules in the asymmetric unit (Table 4) [51]. The molecular structure of both complexes is analogous to that of the **63*S*** above. The molecules of **66*R*** are linked through hydrogen bonds between the coordinated H_2O molecule and one of the nitrato O-atoms. Ac susceptibility measurements for **66*R*** under 4 kOe dc field showed two maxima at the χ'' vs. T plots, which are consistent with two relaxation processes following the Orbach pathway. The data were fitted to the Arrhenius equation for the low- and high-temperature relaxations (Table 4). The complexes show chiroptical activity and circularly polarized luminescence (CPL) in dmf solution, and also magnetic circular dichroism (MCD) signals at r.t. in the range 280–600 nm with g_{max}(MCD)~6.7 $\times$ 10^{-2} T^{-1} attributed to the large orbital angular momentum of aromatic π-conjugated systems (Figure 15). These results suggest that the complexes may have potential applications in magnetochiral devices. The CPL spectra of both complexes show mirror images in the range 430–600 nm, with the g_{PL} for the two enantiomers being $\pm$2.5 $\times$ 10^{-3} (Figure 16).

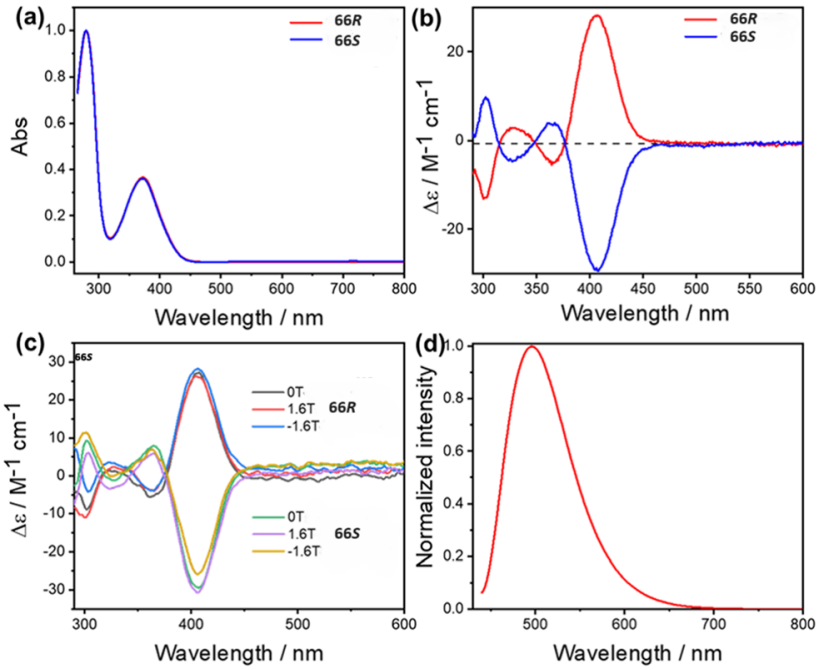

Figure 15. (**a**) UV–visible absorption spectra of **66*R*** and **66*S*** (298 K, DMF). (**b**) CD spectra of **66*R*** and **66*S*** (H = 0, +1.6, and −1.6 T) in the ranges of 270–600 nm at a concentration of 0.05 g L^{-1} (298 K, DMF). (**c**) CD spectra of **66*R*** and **66*S*** at 0.05 g L^{-1} (298 K, DMF). (**d**) PL spectra of **66*R***. Reproduced from Ref. [51] with permission from the Royal Society of Chemistry.

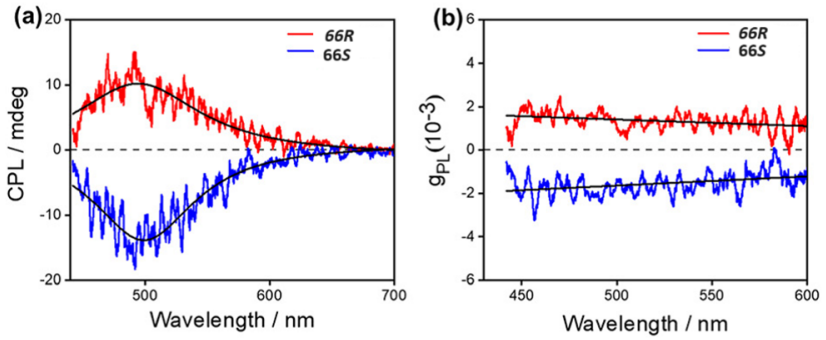

Figure 16. Optical properties of **66*R*/66*S*** measured at room temperature. (**a**) Circularly polarized luminescence emission spectra. (**b**) g_{PL} vs. wavelength curves. Reproduced from Ref. [51] with permission from the Royal Society of Chemistry.

Complexes [ZnLn(L10)$(NO_3)_2(O_2CMe)$] (Ln^{III} = Nd (**67*S***), Dy (**68*R*/68*S***), Yb (**69*R*/69*S***)) were also reported (Table 4) [52–54]. In all complexes, the Zn^{II} ion is located in the $(O_{phenoxo}N_{imino})_2$ pocket of $(L10)^{2-}$ and the Ln^{III} ion is coordinated to the $(O_{phenoxo}O_{methoxo})_2$ donor set and to two chelate nitrato groups. In addition, a bridging μ_2-O_2CMe links the two metal ions. The Zn^{II} ion displays square pyramidal geometry, and the Ln^{III} ion is nine-coordinated with intermediate geometry between the spherical capped square antiprism and the spherical tricapped trigonal prism. Complex **67*S*** displays near-infrared luminescence in MeOH solution [52]. The pair of enantiomers **68*R*/68*S*** were justified by solid-state CD spectroscopy. Both enantiomers display field-induced SIM behavior. Under 1.5 kOe external dc field, two relaxation processes are observed in the frequency and temperature dependences of the ac susceptibilities (Figure 17a). The fit of the data to the Arrhenius law gave the values given in Table 4 for the low- and the high-temperature relaxation, respectively. Polarization measurements as a function of the applied electric field on single crystals showed a hysteresis loop in the *P* vs. *E* curve at 400 K with a large

coercitive field of ~17 kVcm^{-1} with polarization P_s~9.1 μCcm^{-2}, which is comparable to other molecular ferroelectrics (Figure 17b, Table 5) [53]. The molecular crystals of **69*R*/69*S*** display electrical bistability up to 573 K, which is the highest temperature reported for molecular ferroelectric materials. Moreover, this complex also exhibits optical activity, high- and low-temperature luminescence, para- and super-paramagnetic behavior at high- and low-temperature, respectively. The chiral complexes **69*R*/69*S*** also display ferroelectric behavior and room temperature magnetoelectric coupling, therefore combining magnetic and electric polarizabilities in the same phase [54].

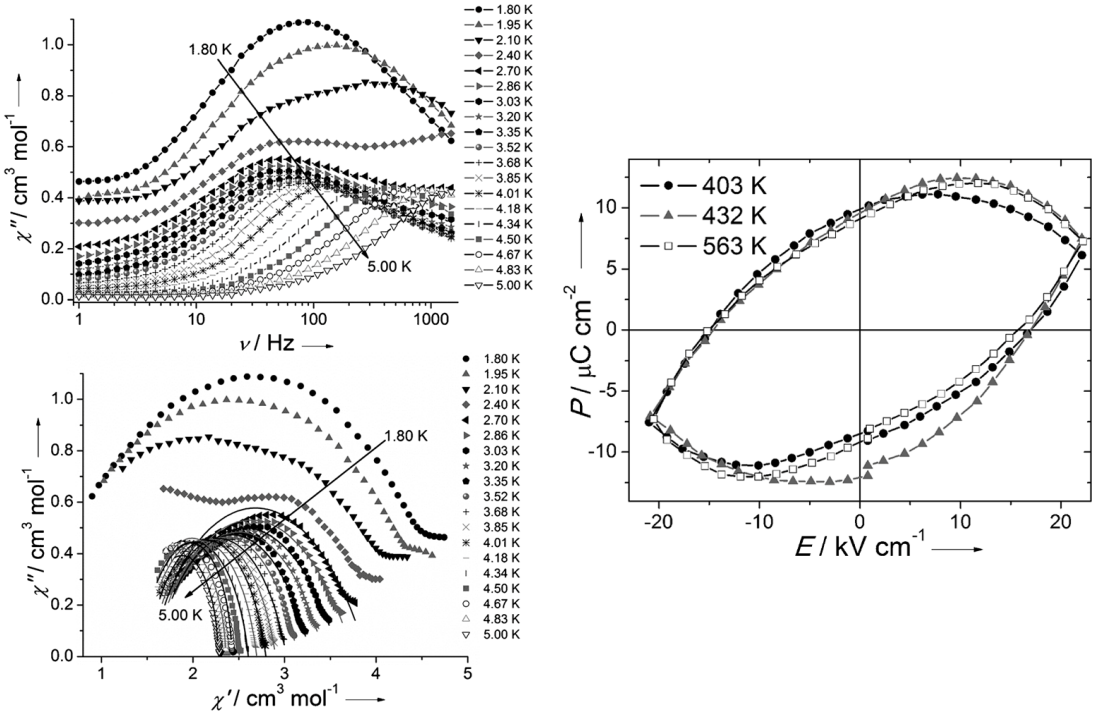

Figure 17. (**a**) Top: Frequency dependence of the out-of-phase (χ'') susceptibility at different temperatures performed under a 1.5 kOe dc field for **68*R***. Bottom: Cole-Cole plot for **68*R*** obtained using the ac susceptibility data (1.5 kOe). The solid lines correspond to the best fit obtained with a generalized Debye model. (**b**) Dielectric hysteresis loop (1 Hz) for **68*R*** obtained from a single crystal at different temperatures [53]. © 2015 WILEY-VCH Verlag GmbH & Co. KGaA, Weinheim.

The enantiopure ligand H_2L11_{RR} (Scheme 1) gave the chiral complex [CuGd($L11_{RR}$)(NO_3)$_3$] (**70*R***), Table 3, [55]. The molecular structure consists of a square planar Cu^{II} ion located in the ($O_{phenoxo}N_{imino}$)$_2$ compartment of $(L11_{RR})^{2-}$ and a ten-coordinated Gd^{III} ion bound to the ($O_{phenoxo}O_{methoxo}$)$_2$ donor set of $(L11_{RR})^{2-}$ and to three chelate nitrato groups. The chiral complex exhibits efficiency in second harmonic generation 0.3 times that of urea. The magnetic susceptibility studies revealed ferromagnetic coupling between the metal ions with exchange parameter J = 1.3 cm^{-1} (g_{Cu} = 2.10, g_{Gd} = 2.01).

The enantiopure ligand H_2L13_{SS} (Scheme 2) gave the chiral complex [ZnNd($L13_{SS}$)(NO_3)$_3$(dmf)$_2$] (**71*S***), Table 4, [52]. The Zn^{II} ion is five-coordinated to the two $O_{phenoxo}$ and two N_{imino} atoms of $(L13_{SS})^{2-}$ and one dmf molecule, whereas the Nd^{III} is nine-coordinated to three O-atoms of the ligand, two chelate nitrates, one monodentate nitrate, and one dmf molecule. Complex **71*S*** displays near-infrared luminescence in MeOH solution.

A chiral 1D coordination polymer [CuGd($L14_{SS}$)(thd)$_2$]$_n$ (**72*S***) was reported (Hthd = 2,2,6,6-tetramethyl-3,5-heptanedione), Table 3, [56]. The ligand H_2L14_{SS} in shown in Scheme 2. The Cu^{II} ion is square planar and is coordinated to the ($O_{phenoxo}N_{imino}$)$_2$ donor atoms of the ligand. This subunit acts as a metalloligand to the two Gd^{III} ions, Gd(1)

and Gd(2). The two $O_{phenoxo}$ and the one $O_{methoxo}$ atoms coordinate at one side of the Gd^{III} ion as a tridentate ligand. The O_{amido} coordinates with another Gd^{III} ion as a monodentate ligand. The eight-coordination of each Gd^{III} ion is completed by two bidentate thd^- ligands (Figure 18). The chiral 1D chains extend along the *b* axis. The magnetic studies revealed ferromagnetic coupling between the metal ions, compatible with spin $S = 4$ in the ground state.

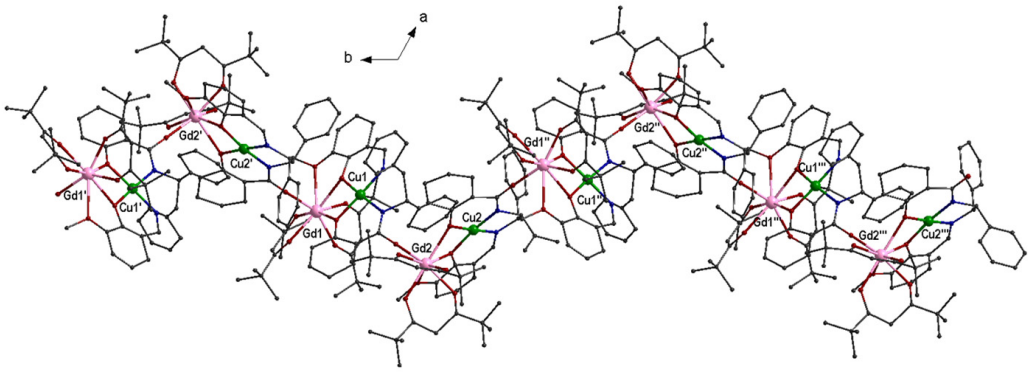

Figure 18. Part of the chiral 1D chain of **72*S***, CCDC-733874, [56]. Color code: Gd pink, Cu green, O red, N blue, C grey. Symmetry operations: (′) $1 - x, 1 - x + y, 5/3 - z$; (″) $1 - x, -x + y, 5/3 - z$; (‴) $x, -1 + y, z$.

The macrocycle enantiopure ligand H_6L16_{RR} (Scheme 3) gave the chiral complex $[Zn_3Er(L16_{RR})(O_2CMe)(NO_3)_2(H_2O)_{1.5}(MeOH)_{0.5}]$ (**73*R***), Table 4, [57]. Each Zn^{II} ion is five-coordinated to two $O_{phenoxo}$ and two N_{imino} atoms from $(L16_{RR})^{6-}$ and one monodentate acetate, nitrate, or methanol ligands at the apical position of a square pyramid. The Er^{III} ion is nine-coordinated to the six $O_{phenoxo}$ atoms of the ligand at equatorial positions, one bidentate nitrate, and a H_2O molecule at apical sites. Complex **73*R*** displays field-induced SIM behavior under 1.0 kOe external dc field (Figure 19).

Table 3. Structural, CD, and magnetic data for the heterometallic Cu/4f complexes.

Complex	3d/4f Ions	Space Group	Coordination Number	CD, λ_{max} (nm)	$\chi_M T$ (r.t.) (cm^3Kmol^{-1})	U_{eff} (K)	t_0 (s)	Ref.
11*R*	Cu/Ce	*P*1	11	−290, −380, +600 [a]	1.05	-	-	[39]
12*R*	Cu/Nd	*P*1	11	−290, −380, +600 [a]	1.52	-	-	[39]
13*R*	Cu/Sm	$P2_1$	10	−290, −380, +600 [a]	0.64	-	-	[39]
14*R*	Cu/Eu	*P*1	10	−290, −380, +600 [a]	1.54	-	-	[39]
15*R*/15*R*′	Cu/Gd	*P*1, $P2_1$	10	−290, −380, +600 [a,b]	8.67, 8.22	-	-	[39]
16*R*/16*R*′	Cu/Tb	*P*1, $P2_1$	10	−290, −380, +600 [a,b]	12.35, 13.10	30.02, 26.16 [c]	9.81×10^{-9}, 2.81×10^{-9}	[39]
17*R*/17*R*′	Cu/Dy	*P*1, $P2_1$	10	−290, −380, +600 [a,b]	14.76, 14.45	5.96, 15.72 [c]	3.66×10^{-6}, 1.70×10^{-7}	[39]
18*R*	Cu/Ho	$P2_1$	9, 10	−300, −375, +600	14.05	8.46 [d]	3.03×10^{-7}	[39]
19*R*	Cu/Er	$P2_1$	9, 10	300, −375, +600	10.36	-	-	[39]
20*R*	Cu/Yb	$P2_1$	9, 10	300, −375, +600	2.59	-	-	[39]
33*R*/33*S*	Cu/Tb	*P*1	8	-	25.15	27.60 [c]	2.03×10^{-5}	[43]
40*R*/40*S*	Cu, Fe/Gd	$P2_1$	9	−380, −530, +470, +610 [a]	9.11	-	-	[45]

Table 3. *Cont.*

Complex	3d/4f Ions	Space Group	Coordination Number	CD, λ_{max} (nm)	$\chi_M T$ (r.t.) (cm^3Kmol^{-1})	U_{eff} (K)	t_0 (s)	Ref.
41*R*/41*S*	Cu, Fe/Tb	$P2_1$	9	−380, −530, +470, +610 [a]	14.13	-	-	[45]
42*R*/42*S*	Cu, Fe/Dy	$P2_1$	9	−380, −530, +470, +610 [a]	17.69	-	-	[45]
43*R*	Cu/Eu	$P2_1$	10	-	-	-	-	[46]
44*R*/44*S*	Cu/Gd	$P2_12_12_1$	10	−237, −285, −390, +219, +261, +334 [a]	8.38	-	-	[47]
70*R*	Cu/Gd	$P2_12_12_1$	10	-	8.20	-	-	[55]
72*S*	Cu/Gd	$P3_221$	8	-	8.14	-	-	[56]
79	Cu, Mo/Gd	-	-	-	9.11	-	-	[58]
80	Cu, Mo/Tb	-	-	-	13.50	-	-	[58]
81	Cu, Mo/Dy	$P2_1$	9	-	-	-	-	[58]
82	Cu, W/La	$P2_1$	9	-	0.70	-	-	[58]
83	Cu, W/Gd	$P2_1$	9	-	8.90	-	-	[58]
84	Cu, W/Tb	$P2_1$	9	-	13.20	-	-	[58]
85	Cu, W/Dy	$P2_1$	9	-	-	-	-	[58]
86	Cu, Mo/La	$C2222_1$	10	-	0.76	-	-	[58]
87	Cu, Mo/Pr	-	-	-	-	-	-	[58]

[a] the values correspond to the *R*-enantiomer, same values with opposite sings correspond to the *S*-enantiomer; [b] for **15*R*′-17*R*′** the λ_{max} values are −300, −375, +600 nm; [c] under 2.0 kOe external dc field; [d] under zero dc field.

Table 4. Structural, CD, and magnetic data for the heterometallic Zn/4f complexes.

Complex	3d/4f Ions	Space Group	Coordination Number	CD, λ_{max} (nm)	$\chi_M T$ (r.t.) (cm^3Kmol^{-1})	U_{eff} (K)	t_0 (s)	Ref.
32*R*	Zn/Lu	*P*1	9	-	-	-	-	[40]
34*R*	Zn/Dy	*P*1	9	−305, −372	14.19	212.1 [b]	7.0×10^{-10}	[44]
35*R*	Zn/Dy	*P*1	9	−310, −386	14.21	203.5 [c]	1.0×10^{-10}	[44]
36*R*	Zn/Dy	*P*1	9	−290, −409	14.18	207.3 [c]	1.5×10^{-5}	[44]
37*S*	Zn/Dy	*P*1	9	+305, +372	28.36	194.5 [b]	3.1×10^{-9}	[44]
38*S*	Zn/Dy	*P*1	9	+310, +386	28.33	70.1/231.6 [c]	8.0×10^{-7}/5.4×10^{-10}	[44]
39*S*	Zn/Dy	*P*1	9	+290, +409	28.40	218.1 [c]	3.5×10^{-11}	[44]
49*R*/49*S*	Zn/Y	$P2_1$	6	-	-	-	-	[49]
50*R*/50*S*	Zn/Lu	$P2_1$	6	-	-	-	-	[49]
51*R*/51*S*	Zn/Dy	$P2_1$	6	-	-	-	-	[49]
52*R*/52*S*	Zn/Sm	$P2_1$	6	-	-	-	-	[49]
53*R*/53*S*	Zn/La	$P2_1$	6	-	-	-	-	[49]
60*R*	Zn/Ce	$P2_1$	10	-	-	4.7 [d]	2.5×10^{-5}	[50]
61*R*	Zn/Nd	$P2_1$	10	-	-	15.9 [e]	3.7×10^{-6}	[50]
62*R*/62*S*	Zn/Eu	$P2_1$	10	−235, −300, +218, +265, +342, +395 [a]	-	-	-	[50]
63*S*	Zn/Dy	$P2_1$	10	-	-	17.7 [e]	8.3×10^{-7}	[50]
64*S*	Zn/Er	$P2_1$	10	-	-	-	-	[50]
65*S*	Zn/Yb	$P2_1$	10	-	-	-	-	[50]
66*R*/66*S*	Zn/Dy	$P2_1$	10	−301, −360, +406 [a]	14.49	11.9/46.1 [f]	4.23×10^{-5}/8.85×10^{-8}	[51]
67*S*	Zn/Nd	$P2_1$	9	-	-	-	-	[52]
68*R*/68*S*	Zn/Dy	$P2_1$	9	−262, −303, +382 [a]	13.44	19.40/51.82 [g] 20.48/51.72 [h]	1.23×10^{-8}/3.75×10^{-9} 8.97×10^{-9}/3.55×10^{-9}	[53]
69*R*/69*S*	Zn/Tb	$P2_1$	9	−261, −303, +386 [a]	-	-	-	[54]
71*S*	Zn/Nd	*C*2	9	-	-	-	-	[52]
73*R*	Zn/Er	$P2_12_12_1$	9	-	-	8.1 [i]	5.3×10^{-7}	[57]

[a] the values correspond to the *R*-enantiomer, same values with opposite sings correspond to the *S*-enantiomer; [b] under 1.8 kOe external dc field, n = 5.49, C = 1.6×10^{-3} $s^{-1}K^{-5.49}$ (**34*R***), n = 5.72, C = 7.6×10^{-4} $s^{-1}K^{-5.72}$ (**37*S***); [c] under 2.0 kOe external dc field, n = 5.06, C = 1.2×10^{-2} $s^{-1}K^{-5.06}$ (**35*R***), n = 5.29, C = 1.9×10^{-2} $s^{-1}K^{-5.29}$ (**36*R***), n = 4.54, C = 3.9×10^{-2} $s^{-1}K^{-4.54}$ for the slow relaxation and n = 5.98, C = 1.8×10^{-4} $s^{-1}K^{-5.98}$ for the fast relaxation (**38*S***), n = 4.78, C = 5.4×10^{-2} $s^{-1}K^{-4.78}$ (**39*S***); [d] under 0.5 kOe external dc field; [e] under 1.0 kOe external dc field; [f] under 4.0 kOe external dc field, for the low- and high-temperature relaxation; [g] under 1.5 kOe external dc field for the *R*-enantiomer, for the low- and high-temperature relaxation; [h] under 1.5 kOe external dc field for the *S*-enantiomer, for the low- and high-temperature relaxation; [i] under 1.0 kOe external dc field.

Table 5. Ferroelectric and spectroscopic data for the chiral 4f and 3d/4f complexes.

Complex	P_r (μCcm^{-2})	E_c ($kVcm^{-1}$)	UV-Vis (nm)	Fluorescence (nm)	MCD g_{max} (T^{-1})	CPL g_{PL}	SHG, $\chi_R^{(2)}$ (pmV^{-1})	THG, $\chi_R^{(3)}$ (pm^2V^{-2})	Ref.
6*R*	4.51	28.11	-	-	-	-	-	-	[35]
7*S*	7.98	22.12	-	-	-	-	-	-	[36]
32*R*	-	-	-	460	-	-	-	-	[40]
34*R*	-	-	-	-	-	-	0.04	581	[44]
35*R*	-	-	-	-	-	-	0.01	821	[44]
36*R*	-	-	-	-	-	-	0.07	848	[44]
37*S*	-	-	-	-	-	-	0.39	485	[44]
38*S*	-	-	-	-	-	-	0.02	703	[44]
39*S*	-	-	-	-	-	-	0.40	718	[44]
66*R*/66*S*	-	-	279, 372	490	6.7×10^{-2}	$\pm 2.5 \times 10^{-3}$	-	-	[51]
68*R*	9.1	17.0	-	-	-	-	-	-	[53]
70*R*	-	-	310	-	-	-	-	-	[55]

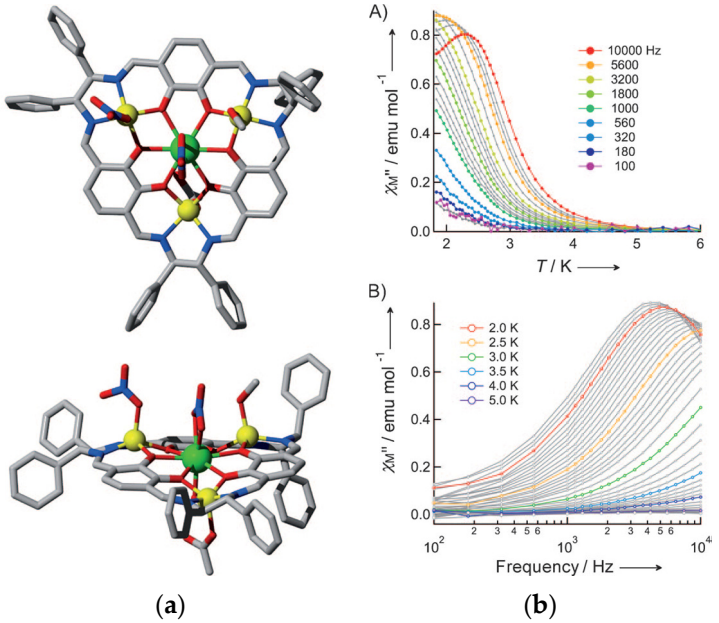

Figure 19. (**a**) Top view (top) and side view (bottom) of the molecular structure of **73*R***. Color code: Er gree, Zn yellow, O red, N blue, C light grey. (**b**) (A) Temperature and (B) frequency dependence of χ_M'' values of **73*R*** measured under 1.0 kOe external field. The solid curves are guides for the eye [57]. Copyright © 2011 WILEY-VCH Verlag GmbH & Co. KGaA, Weinheim.

4. Chiral Materials from Racemic Salen-Type Schiff Base Ligands

The condensation reaction of 2-hydroxy-benzaldehyde (salicylaldehyde) with 1,2-diamino-cyclohexane gave the Schiff base ligand H_2L1 (Scheme 1) which upon reaction with $Ce(NO_3)_3 \cdot 6H_2O$ in EtOH gave complex $[Ce^{IV}(L1)_2]$ (**74**) which crystallizes in the chiral monoclinic space group $P2_1$ [34]. The absolute structure was determined by the Flack parameter, x = 0.53(4), which indicates racemic twinning. The absolute configuration of both chiral centers in $L(1)^{2-}$ is *R*,*S*- and due to racemic twinning, the *S*,*R*- also exist in the crystal structure. The Ce^{IV} ion is eight-coordinated to the two $O_{phenoxo}$ and the two N_{imino} atoms from two $(L1)^{2-}$ ligands with Ce-O and Ce-N distances in range 2.148(7)-2.241(9) Å and 2.525(11)-2.619(9) Å, respectively. The best planes of the coordination spheres of the two ligands form a dihedral angle of 87.7(3)°. The coordination geometry is best described as snub diphenoid (JSD-8, CShM = 1.31927).

The zwitterion of racemic H_2L1 forms 3D coordination polymers $[Ln^{III}Cl(NO_3)_2(H_2L1)]_n$ (Ln^{III} = La (**75**), Ce (**76**), Nd (**77**)) [59,60] which crystallize in the tetragonal chiral space group $P4_32_12$ with diamond (*dia*) network topology (Figure 20). The Ln^{III} ion is nine-coordinated to two chelate nitrato and one chlorido group, as well as to four $O_{phenoxo}$ atoms from four different H_2L1 zwitterions. The coordination polyhedron around the Ln^{III} ion is a tricapped trigonal prism (JTCTPR-9). The 3D structure is built by $[Ln^{III}(H_2L1)]^{3+}$ subunits, with the Ln^{III} ion and the H_2L1 serving as the head and tail, respectively, of a tadpole-like model, with all the tails being right-handed. In this head-to-tail ligation mode, the tadpole-like models link each other and form two 1D right-handed helical chains, each one directed along the *a* and *b* axis. Two such helixes interweave each other by sharing the Ln^{III} ions, thus forming the *dia* 3D network. Compounds **75–77** contain the enantiopure H_2L1_{SS} ligand due to the trans orientation of the ligand, which shows higher stability and lower steric hindrance, and also due to hydrogen bonds which stabilize the structure. Compounds **75–77** represent the first 3D chiral lanthanide MOFs with *dia* topology and opened new ways for the synthesis of enantiopure materials from racemate precursors. The chirality of these MOFs results in the SHG effects, and they are the first examples of NLO-active enantiopure Ln-salen frameworks.

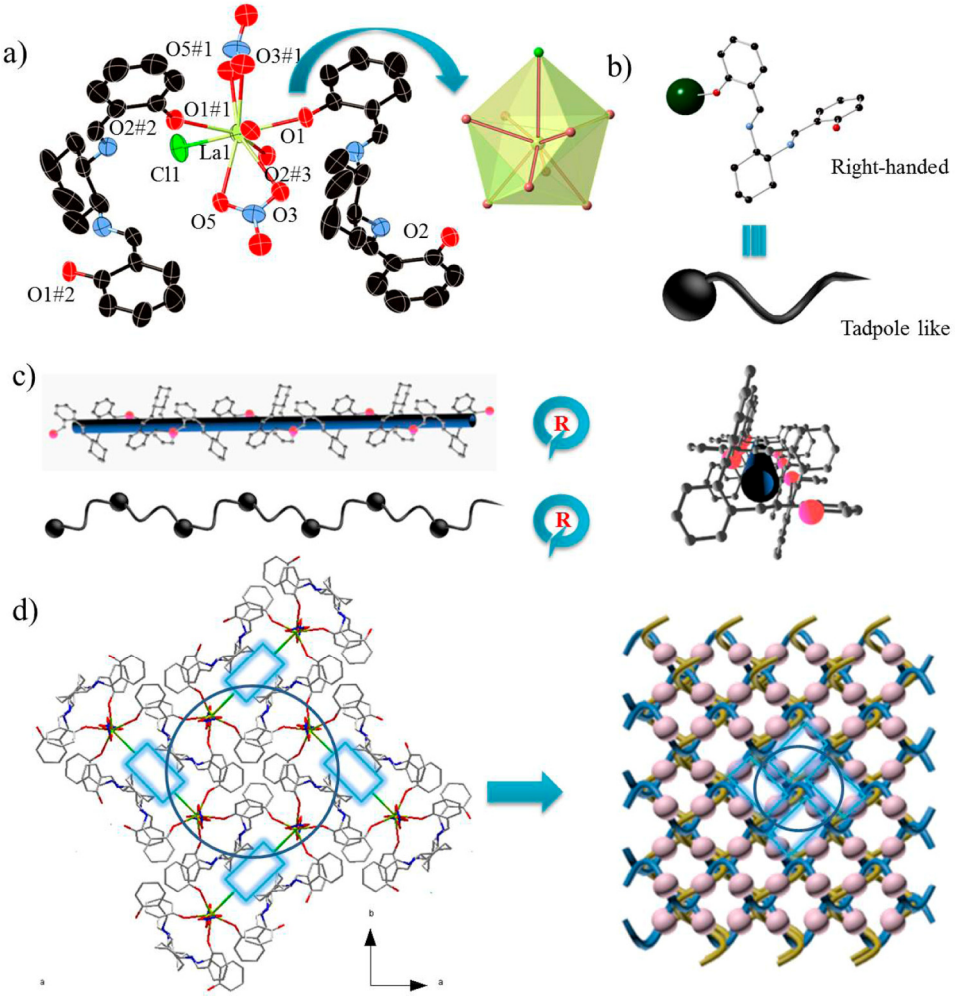

Figure 20. Crystal structure of **75**: (**a**) the structural unit, #1, y, x, $2 - z$; #2, $0.5 - x$, $-0.5 + y$, $1.75 - z$; #3, $-0.5 + y$, $0.5 - x$, $0.25 + z$; (**b**) tadpole-like metal-organic subunit; (**c**) combined ball and stick and cartoon representation of the 1D right-handed helical chain (hydrogen atoms are omitted for clarity); (**d**) combined ball and stick and cartoon representation of the 3D open metal-organic framework [60]. Copyright © 2014, American Chemical Society.

The use of the zwitterion of racemic ligand H_2L2 (Scheme 1) gave the 3D polymer $\{[Ce^{III}(H_2L2)(NO_3)_2](PF_6)\}_n$ (**78**), which crystallizes in the hexagonal chiral space group $P6_422$ with quartz (**qtz**) topology [61]. The structure consists of right-handed helixes of $[Ce^{III}(H_2L2)]_n$. The Ce^{III} ion is eight-coordinated to four $O_{phenoxo}$ atoms from four different H_2L2 ligands and to two chelate nitrato groups in a hexagonal bipyramid geometry (HB PY-8, CShM = 7.53410, Figure 21).

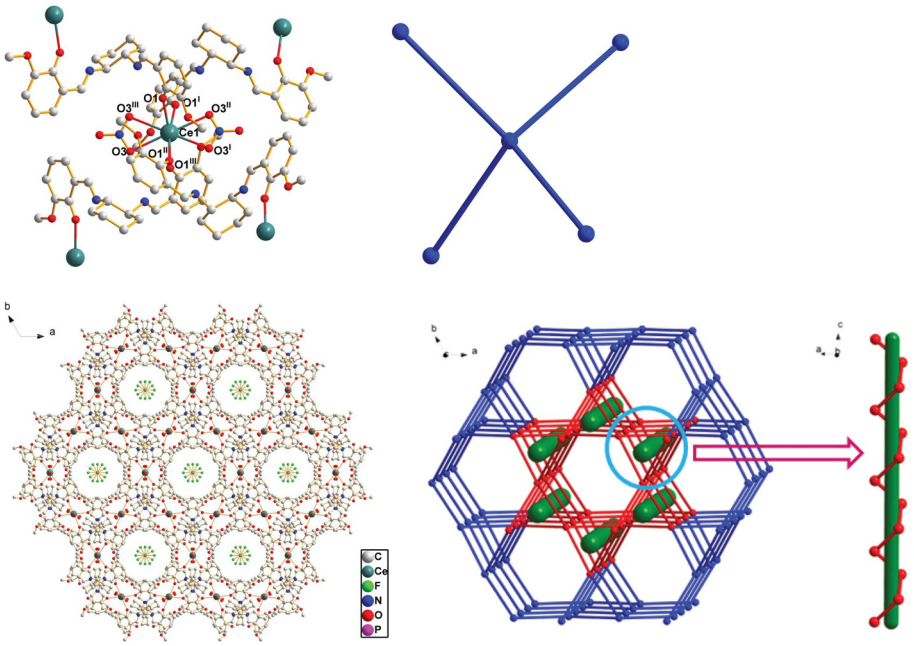

Figure 21. (**top**) The coordination environment of Ce^{III} ion (left) and the simplified ball and stick model (right, the blue lines represent the salen type ligand) in the cation of **78** (H-atoms are omitted for clarity). Symmetry codes: (i) x, $x - y + 1$, $-z + 3/2$; (ii) $-x$, $-x + y$, $-z + 3/2$; (iii) $-z$, $-y + 1$, z. (**bottom**) 3D coordination structure of **78** along the c axis (left) and schematic illustration of quartz topology with the Schläfli symbol $\{64{\cdot}8^2\}$ along the c axis (right, the free PF_6^- ions are omitted for clarity). Reproduced from Ref. [61] with permission from the Royal Society of Chemistry.

The racemic ligand H_2L15 (Scheme 2) gave the chiral 1D coordination polymers $[\{CuLn(L15)(H_2O)_4\}\{M(CN)_8\}]_n$ (M^V = Mo, Ln^{III} = Gd (**79**), Tb (**80**), Dy (**81**); M^V = W, Ln^{III} = La (**82**), Gd (**83**), Tb (**84**), Dy (**85**)) and $[\{Cu_2Ln(L15)_2(H_2O)_4\}\{Mo(CN)_8\}]$ (Ln^{III} = La (**86**), Pr (**87**)) [58]. The polymeric structure of **81–85** is based on $\{M(CN)_8\}$ units coordinated through one cyano ligand to the Cu^{II} ion of a dinuclear {CuLn} moiety. The $\{Cu^{II}Ln^{III}M^V\}$ fragment is further linked through a second cyano group to the Ln^{III} ion of an adjacent trimetallic fragment (Figure 22, Table 3). The $(L15)^{2-}$ ligand is coordinated via the two $O_{phenoxo}$ and the N_{imino} atoms to the Cu^{II} ion and through the two bridging $O_{phenoxo}$ and the two $O_{methoxo}$ to the Ln^{III}. The nine-coordination of the latter is completed by four aqua ligands and one nitrogen atom from the cyano bridge. The coordination geometry is distorted monocapped square antiprism. Intermolecular O···O and N···O type hydrogen bonds, involving the free cyano groups, the crystallization, and coordinated H_2O molecules, establish a 3D supramolecular network. The structure of **86** is based on trinuclear $\{Cu^{II}_2(L15)_2La^{III}\}$ moieties linked by $\{Mo(CN)_8\}^{3-}$ anions, resulting in 1D chains running along the crystallographic c axis. There are two C2 axes passing through La^{III} and Mo^V; thus, half of the $[\{CuLa(L15)(H_2O)_4\}\{Mo(CN)_8\}]$ repeating unit is independent (Figure 23). The structure of the trinuclear $\{Cu^{II}_2(L15)_2La^{III}\}$ moiety consists of a central La^{III} ion, which is bound to the $(O_{phenoxo}O_{methoxo})_2$ donor set from the two $(L15)^{2-}$ ligands, whereas each of the Cu^{II} ions is hosted in the $(O_{phenoxo}N_{imino})_2$ pocket of each $(L15)^{2-}$ ligand. The ten-coordination around the La^{III} ion is completed from cyano bridges and is described as distorted bicapped square antiprism. Each Cu^{II} ion is five-coordinated with

one cyano bridge in the apical position of the square pyramid. The chains of **86** are linked through C-H···π intermolecular interactions and form a 3D supramolecular network.

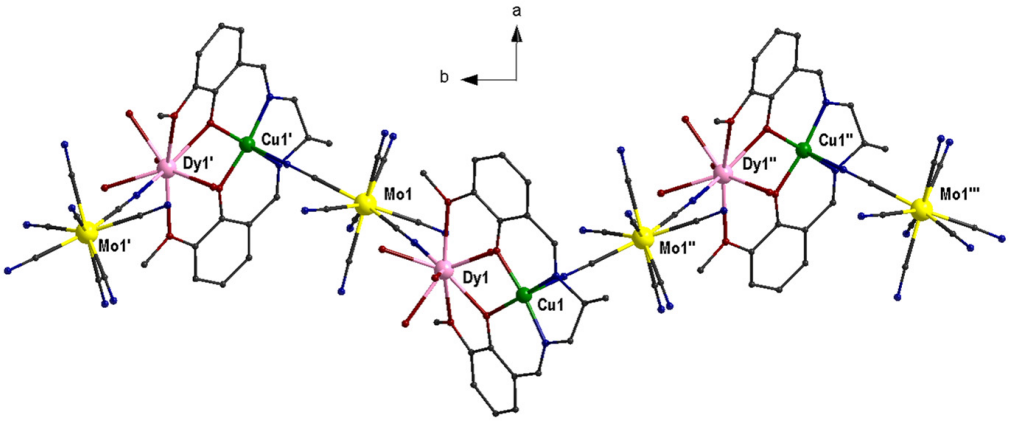

Figure 22. Part of the chiral zigzag chain of **81**, CCDC-1060179, [58]. Color code: Dy pink, Mo yellow, Cu green, O red, N blue, C grey. Symmetry operations: (′) $1 - x$, $0.5 + y$, $1 - z$; (″) $1 - x$, $-0.5 + y$, $1 - z$; (‴) x, $-1 + y$, z.

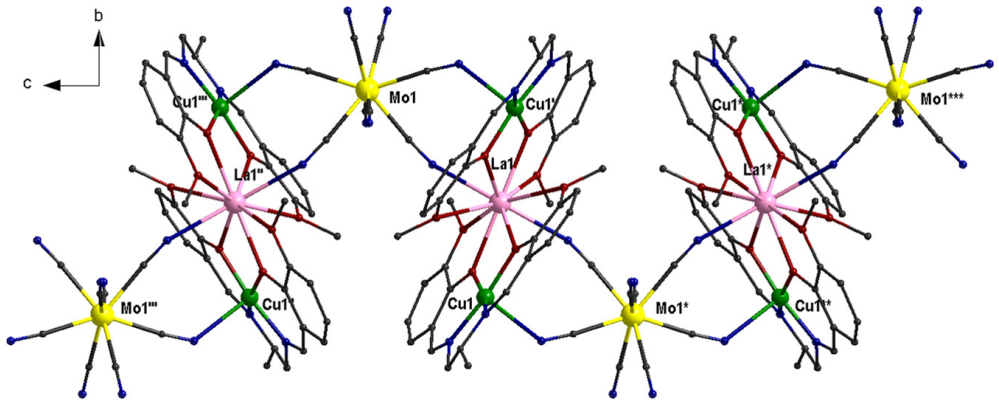

Figure 23. Part of the chiral zigzag chain of **86**, CCDC-1060184, [58]. Color code: La pink, Mo yellow, Cu green, O red, N blue, C grey. Symmetry operations: (′) $-x$, $-y$, $-z$; (″) $-x$, y, $0.5 - z$; (‴) $-x$, $-y$, $0.5 + z$; (*) $-x$, $-y$, $-0.5 + x$; (**) $-x$, y, $-0.5 + z$; (***) x, y, $-1 + z$.

5. Concluding Comments

The enantiopure Schiff base ligands depicted in Schemes 1–3 gave homometallic 4f and heterometallic 3d-4f chiral complexes with diverse nuclearities, metal topologies, coordination geometries, and physical properties. In the homometallic 4f complexes **1–8**, the Ln^{III} ion is coordinated to the $O_{phenoxo}/N_{imino}$ atoms of the Schiff base ligand, whereas in complexes **9** and **10**, which contain the ligand in the zwitterion form, the lanthanide is bound to the $O_{phenoxo}$ and/or $O_{methoxo}$ atoms. In the 4f complexes **1–10**, the Ln^{III} ions display coordination numbers, which range from seven to ten. In the heterometallic 3d-4f complexes **11–73**, the 3d metal ions are coordinated to the Schiff base ligands through the $O_{phenoxo}/N_{imino}$ atoms in square planar geometry. In some cases, five- or six-coordination is observed from coordinated co-ligands, such as solvent molecules, organic or inorganic anions, and the 3d ions display square planar or octahedral geometries. In complexes **11–73**, the lanthanide ions are coordinated via the $O_{phenoxo}/O_{alkoxo}$ atoms of the ligands; the $O_{phenoxo}$ atoms serve as bridging atoms between the 3d and 4f ions. The coordination environment of the Ln^{III} ions is completed by co-ligands, such as nitrates, azides, and carboxylates, and gives coordination numbers from six to eleven. In the chiral complexes **74–86** derived from racemic Schiff bases, the Ln^{III} ions are coordinated to the $O_{phenoxo}/N_{imino}$ atoms, or to the $O_{phenoxo}/O_{alkoxo}$ atoms, or to the $O_{phenoxo}$ atoms, depending on the simultaneous

presence of other metal ions, or the coordination diversity of the ligand which promotes the formation of network structures.

The chiral complexes discussed herein constitute multifunctional molecular materials that combine chirality with various physical properties. The majority of the complexes display field-induced slow magnetic relaxation compatible with single-ion magnetic behavior. This behavior was observed in complexes of oblate ions, such as Tb^{III}, Dy^{III}, and Ho^{III}, prolate ions, such as Yb^{III}, and of 'uncommon magnetic lanthanides', Ce^{III}, and Nd^{III}. Other physical properties, such as ferroelectric, optical, catalytic, and anticancer behavior, were reported.

Funding: This research received no external funding.

Data Availability Statement: Data available in a publicly accessible repository.

Conflicts of Interest: The author declares no conflicts of interest.

References

1. Bruce, D.W.; O'Hare, D.; Walton, R.I. (Eds.) *Molecular Materials*; Wiley: Hoboken, NJ, USA, 2011.
2. Coronado, E. Molecular magnetism: From chemical design to spin control in molecules, materials and devices. *Nat. Rev. Mater.* **2020**, *5*, 87–194. [CrossRef]
3. Atzori, M.; Artizzu, F. (Eds.) *Functional Molecular Materials: An Introductory Textbook*; Pan Stanford Publishing, Pte. Ltd.: Singapore, 2018.
4. Ouahab, L. *Multifunctional Molecular Materials*; Pan Stanford Publishing, Pte. Ltd.: Singapore, 2013.
5. Mamula, O.; von Zelewsky, A. Supramolecular coordination compounds with chiral pyridine and polypyridine ligands derived from terpenes. *Coord. Chem. Rev.* **2003**, *242*, 87–95. [CrossRef]
6. Bauer, E.B. Chiral-at-metal complexes and their catalytic applications in organic synthesis. *Chem. Soc. Rev.* **2012**, *41*, 3153–3167. [CrossRef] [PubMed]
7. Knof, U.; von Zelewsky, A. Predetermined chirality at metal centers. *Angew. Chem. Int. Ed. Engl.* **1999**, *38*, 302–322. [CrossRef]
8. Mukhtar, S.D.; Suhail, M. Chiral metallic anticancer drugs: A brief-review. *Eur. J. Chem.* **2022**, *13*, 483–490. [CrossRef]
9. Anthony, E.J.; Bolitho, E.M.; Bridgewater, H.E.; Carter, O.W.L.; Donnelly, J.M.; Imberti, C.; Lant, E.C.; Lermyte, F.; Needham, R.J.; Palau, M.; et al. Metallodrugs are unique: Opportunities and challenges of discovery and development. *Chem. Sci.* **2020**, *11*, 12888–12917. [CrossRef]
10. Li, D.-P.; Wang, T.-W.; Li, C.-H.; Liu, D.-S.; Li, Y.-Z.; You, X.-Z. Single-ion magnets based on mononuclear lanthanide complexes with chiral Schiff base ligands $[Ln(FTA)_3L]$ (Ln = Sm, Eu, Gd, Tb and Dy). *Chem. Commun.* **2010**, *46*, 2929–2931. [CrossRef]
11. Guo, P.-H.; Liu, J.-L.; Jia, J.-H.; Wang, J.; Guo, F.-S.; Chen, Y.-C.; Lin, W.-Q.; Leng, J.-D.; Bao, D.-H.; Zhang, X.-D.; et al. Multifunctional Dy^{III}_4 cluster exhibiting white-emitting, ferroelectric and single-molecule magnet behavior. *Chem. Eur. J.* **2013**, *19*, 8769–8773. [CrossRef]
12. Wen, H.-R.; Hu, J.-J.; Yang, K.; Zhang, J.-L.; Liu, S.-J.; Liao, J.-S.; Liu, C.-M. Family of chiral Zn^{II}-Ln^{III} (Ln = Dy and Tb) heterometallic complexes derived from the amine-phenol ligand showing multifunctional properties. *Inorg. Chem.* **2020**, *59*, 2811–2824. [CrossRef]
13. Liu, C.-M.; Zhang, D.-Q.; Xiong, R.-G.; Hao, X.; Zhu, D.-B. A homochiral Zn-Dy heterometallic left-handed helical chain complex without chiral ligands: Anion-induced assembly and multifunctional integration. *Chem. Commun.* **2018**, *54*, 13379–13382. [CrossRef]
14. Wang, K.; Zeng, S.; Wang, H.; Dou, J.; Jiang, J. Magneto-chiral dichroism in chiral mixed (phthalocyaninato)(porphyrinato) rare earth triple-decker SMMs. *Inorg. Chem. Front.* **2014**, *1*, 167–171. [CrossRef]
15. Atzori, M.; Dhbaibi, K.; Douib, H.; Grasser, M.; Dorcet, V.; Breslavetz, I.; Paillot, K.; Cador, O.; Rikken, G.L.J.A.; Le Guennic, B.; et al. Helicene-based ligands enable strong magneto-chiral dichroism in a chiral ytterbium complex. *J. Am. Chem. Soc.* **2021**, *143*, 2671–2675. [CrossRef] [PubMed]
16. Liu, C.-M.; Sun, R.; Wang, B.-W.; Wu, F.; Hao, X.; Shen, Z. Homochiral Ferromagnetic Coupling Dy_2 single-molecule magnets with strong magneto-optical Faraday effects at room temperature. *Inorg. Chem.* **2021**, *60*, 12039–12048. [CrossRef] [PubMed]
17. Wang, X.; Du, M.-H.; Xu, H.; Long, L.-S.; Kong, X.-J.; Zheng, L.-S. Cocrystallization of chiral 3d-4f clusters $\{Mn_{10}Ln_6\}$ and $\{Mn_6Ln_2\}$. *Inorg. Chem.* **2021**, *60*, 5925–5930. [CrossRef] [PubMed]
18. Lefeuvre, B.; Mattei, C.A.; Gonzalez, J.F.; Gendron, F.; Dorcet, V.; Riobé, F.; Lalli, C.; Guennic, B.L.; Cador, O.; Maury, O.; et al. Solid-state near-infrared circularly polarized luminescence from chiral Yb^{III}-single-molecule magnet. *Chem. Eur. J.* **2021**, *27*, 7362–7366. [CrossRef] [PubMed]
19. El Rez, B.; Liu, J.; Béreau, V.; Duhayon, C.; Horino, Y.; Suzuki, T.; Coolen, L.; Sutter, J.-P. Concomitant emergence of circularly polarized luminescence and single-molecule magnet behavior in chiral-at-metal Dy complex. *Inorg. Chem. Front.* **2020**, *7*, 4527–4534. [CrossRef]
20. Woodruff, D.N.; Winpenny, R.E.P.; Layfield, R.A. Lanthanide single-molecule magnets. *Chem. Rev.* **2013**, *113*, 5110–5148. [CrossRef] [PubMed]

21. Meng, Y.-S.; Jiang, S.-D.; Wang, B.-W.; Gao, S. Understanding the magnetic anisotropy toward single-ion magnets. *Acc. Chem. Res.* **2016**, *49*, 2381–2389. [CrossRef]
22. Liu, K.; Shi, W.; Cheng, P. Toward heterometallic single-molecule magnets: Synthetic strategy, structures and properties of 3d-4f discrete complexes. *Coord. Chem. Rev.* **2015**, *289–290*, 74–122. [CrossRef]
23. Gupta, S.K.; Rajeshkumar, T.; Rajaraman, G.; Murugavel, R. An air-stable Dy(III) single-ion magnet with high anisotropy barrier and blocking temperature. *Chem. Sci.* **2016**, *7*, 5181–5191. [CrossRef]
24. Liu, J.; Chen, Y.-C.; Liu, J.-L.; Vieru, V.; Ungur, L.; Jia, J.-H.; Chibotaru, L.F.; Lan, Y.; Wernsdorfer, W.; Gao, S.; et al. A stable pentagonal bipyramidal Dy(III) single-ion magnet with a record magnetization reversal barrier over 1000 K. *J. Am. Chem. Soc.* **2016**, *138*, 5441–5450. [CrossRef] [PubMed]
25. Ding, Y.-S.; Chilton, N.F.; Winpenny, R.E.P.; Zheng, Y.-Z. On approaching the limit of molecular magnetic anisotropy: A near-perfect pentagonal bipyramidal dysprosium(III) single-molecule magnet. *Angew. Chem. Int. Ed.* **2016**, *55*, 16071–16074. [CrossRef] [PubMed]
26. Meng, Y.-S.; Xu, L.; Xiong, J.; Yuan, Q.; Liu, T.; Wang, B.-W.; Gao, S. Low-coordinate single-ion magnets by intercalation of lanthanides into a phenol matrix. *Angew. Chem. Int. Ed.* **2018**, *57*, 4763–4766. [CrossRef]
27. Goodwin, C.A.P.; Ortu, F.; Reta, D.; Chilton, N.F.; Mills, D.P. Molecular magnetic hysteresis at 60 kelvin in dysprosocenium. *Nature* **2017**, *548*, 439–442. [CrossRef] [PubMed]
28. Guo, F.-S.; Day, B.M.; Chen, Y.-C.; Tong, M.-L.; Mansikkamäki, A.; Layfield, R.A. Magnetic hysteresis up to 80 kelvin in a dysprosium metallocene single-molecule magnet. *Science* **2018**, *362*, 1400–1403. [CrossRef] [PubMed]
29. Meena, R.; Meena, P.; Kumari, A.; Sharma, N.; Fahmi, N. *Schiff Base in Organic, Inorganic and Physical Chemistry*; Chapter 4; Akitsu, T., Ed.; IntechOpen: London, UK, 2023.
30. Boulechfar, C.; Ferkous, H.; Delimi, A.; Djedouani, A.; Kahlouche, A.; Boublia, A.; Darwish, A.S.; Lemaoui, T.; Verma, R.; Benguerba, Y. Schiff bases and their metal complexes: A review on the history, synthesis, and applications. *Inorg. Chem. Commun.* **2023**, *150*, 110451. [CrossRef]
31. Ceramella, J.; Iacopetta, D.; Catalano, A.; Cirillo, F.; Lappano, R.; Sinicropi, M.S. A review on the antimicrobial activity of Schiff bases: Data collection and recent studies. *Antibiotics* **2022**, *11*, 191. [CrossRef]
32. Ren, M.; Xu, Z.-L.; Wang, T.-T.; Bao, S.-S.; Zheng, Z.-H.; Zhang, Z.-C.; Zheng, L.-M. Homochiral mononuclear Dy-Schiff base complexes showing field-induced double magnetic relaxation processes. *Dalton Trans.* **2016**, *45*, 690–695. [CrossRef]
33. Yao, M.-X.; Zheng, Q.; Gao, F.; Li, Y.-Z.; Song, Y.; Zuo, J.-L. Field-induced slow magnetic relaxation in chiral seven-coordinated mononuclear lanthanide complexes. *Dalton Trans.* **2012**, *41*, 13682–13690. [CrossRef]
34. Szłyk, E.; Wojtczak, A.; Dobrzańska, L.; Barwiołek, M. X-ray crystal structure and nuclear Overhauser effect studies of cerium(IV) complexes with Schiff bases obtained from N,N′-(1*R*,2*R*)(-)-1,2-cyclohexanediamine and benzaldehyde derivatives. *Polyhedron* **2008**, *27*, 765–776. [CrossRef]
35. Sui, Y.; Fang, X.-N.; Hu, R.-H.; Li, J.; Liu, D.-S. A new type of multifunctional single ionic dysprosium complex based on chiral salen-type Schiff base ligand. *Inorg. Chim. Acta* **2014**, *423*, 540–544. [CrossRef]
36. Sui, Y.; Hu, R.-H.; Luo, Z.-G.; Lin, W.-H.; Liu, D.-S. Synthesis, structure and properties of an erbium(iii) complex with chiral salen-type Schiff base ligand. *Z. Anorg. Allg. Chem.* **2015**, *641*, 1566–1570. [CrossRef]
37. Okumura, Y.; Takiguchi, Y.; Nakame, D.; Akitsu, T. Crystal structure and Hirshfeld surface analysis of ((*S*,*S*)-2,2′-{(1,2-diphenylethane-1,2-diyl)bis[(azaniumylylidene) methanylylidene]}bis(6-methoxyphenolato))trinitratosamarium(III). *Acta Cryst.* **2021**, *E77*, 579–582. [CrossRef] [PubMed]
38. Fan, Y.-H.; Wang, A.-D.; Bi, C.-F.; Xiao, Y.; Bi, S.-Y.; Zhang, X.; Wang, Q. Synthesis, crystal structure and anticancer activity of 2D-coordination polymer of cerium(III) with chiral Schiff base trans-*N*,*N*-bis-(2-hydroxy-1-naphthalidehydene)-(1*R*,2*R*)-cyclohexanediamine. *Synth. Met.* **2011**, *161*, 1552–1556. [CrossRef]
39. Wen, H.-R.; Bao, J.; Liu, S.-J.; Liu, C.-M.; Zhang, C.-W.; Tang, Y.-Z. Temperature-controlled polymorphism of chiral Cu^{II}-Ln^{III} dinuclear complexes exhibiting slow magnetic relaxation. *Dalton Trans.* **2015**, *44*, 11191–11201. [CrossRef] [PubMed]
40. Orita, S.; Akitsu, T. Variety of crystal structures of chiral Schiff base Lu(III)-Ni(II)/Cu(II)/Zn(II) and the related complexes. *Open Chem.* **2014**, *1*, 1–14. [CrossRef]
41. Wen, H.-R.; Liu, S.-J.; Xie, X.-R.; Bao, J.; Liu, C.-M.; Chen, J.-L. A family of nickel-lanthanide heterometallic dinuclear complexes derived from a chiral Schiff-base ligand exhibiting single-molecule magnet behaviors. *Inorg. Chim. Acta* **2015**, *435*, 274–282. [CrossRef]
42. Okamoto, Y.; Nidaira, K.; Akitsu, T. Environmental dependence of artifact CD peaks of chiral Schiff base 3d-4f complexes in soft mater PMMA matrix. *Int. J. Mol. Sci.* **2011**, *12*, 6966–6979. [CrossRef] [PubMed]
43. Huang, X.-C.; Vieru, V.; Chibotaru, L.F.; Wernsdorfer, W.; Jiang, S.-D.; Wang, X.-Y. Determination of magnetic anisotropy in a multinuclear Tb^{III}-based single-molecule magnet. *Chem. Commun.* **2015**, *51*, 10373–10376. [CrossRef]
44. Liu, C.-M.; Sun, R.; Wang, B.-W.; Hao, X.; Li, X.-L. Effects of counterions, coordination anions, and coordination solvent molecules on single-molecule magnetic behaviors and nonlinear optical properties of chiral Zn_2Dy Schiff base complexes. *Inorg. Chem.* **2022**, *61*, 18510–18523. [CrossRef]
45. Deng, X.-W.; Cai, L.-Z.; Zhu, Z.-X.; Gao, F.; Zhou, Y.-L.; Yao, M.-X. Synthesis, structures and magnetic properties of chiral 3d–3d′–4f heterotrimetallic complexes based on $[(Tp^*)Fe(CN)_3]^-$. *New J. Chem.* **2017**, *41*, 5988–5994. [CrossRef]
46. Constable, E.C.; Zhang, G.; Housecroft, C.E.; Neuburger, M.; Zampese, J.A. The mononuclear-dinuclear dance: Twisting the backbone in metalloligands operates a coordination switch. *Inorg. Chim. Acta* **2010**, *363*, 4207–4213. [CrossRef]

47. Sui, Y.; Liu, D.-S.; Hu, R.-H.; Huang, J.-G. One-dimensional zigzag chain of Cu-Gd coordination polymers derived from chiral hexadentate Schiff base ligands: Synthesis, structure and magnetic properties. *Inorg. Chim. Acta* **2013**, *395*, 225–229. [CrossRef]
48. Yadav, M.; Bhunia, A.; Jana, S.K.; Roesky, P.W. Manganese- and lanthanide-based 1D chiral coordination polymers as an enantioselective catalyst for sulfoxidation. *Inorg. Chem.* **2016**, *55*, 2701–2708. [CrossRef] [PubMed]
49. Xu, R.; Hua, L.; Li, X.; Yao, Y.; Leng, X.; Chen, Y. Rare-earth/zinc heterometallic complexes containing both alkoxy-amino-bis(phenolato) and chiral salen ligands: Synthesis and catalytic application for copolymerization of CO_2 with cyclohexene oxide. *Dalton Trans.* **2019**, *48*, 10565–10573. [CrossRef] [PubMed]
50. Mayans, J.; Saez, Q.; Font-Bardia, M.; Escuer, A. Enhancement of magnetic relaxation properties with 3d diamagnetic cations in $[Zn^{II}Ln^{III}]$ and $[Ni^{II}Ln^{III}]$, Ln^{III} = Kramers lanthanides. *Dalton Trans.* **2019**, *48*, 641–652. [CrossRef] [PubMed]
51. Huang, H.; Sun, R.; Wu, X.-F.; Liu, Y.; Zhan, J.-Z.; Wang, B.-W.; Gao, S. Circularly polarized luminescence and magnetooptic effects from chiral Dy(III) single molecule magnets. *Dalton Trans.* **2023**, *52*, 7646–7651. [CrossRef] [PubMed]
52. Bi, W.-Y.; Lu, X.-Q.; Chai, W.-L.; Song, J.-R.; Wong, W.-Y.; Wong, W.-K.; Jones, R.A. Construction and NIR luminescent property of hetero-bimetallic Zn-Nd complexes from two chiral salen-type Schiff-base ligands. *J. Mol. Struct.* **2008**, *891*, 450–455. [CrossRef]
53. Long, J.; Rouquette, J.; Thibaud, J.-M.; Ferreira, R.A.S.; Carlos, L.D.; Donnadieu, B.; Vieru, V.; Chibotaru, L.F.; Konczewicz, L.; Haines, J.; et al. A high-temperature molecular ferroelectric Zn/Dy complex exhibiting single-ion-magnet behavior and lanthanide luminescence. *Angew. Chem. Int. Ed. Engl.* **2015**, *54*, 2236–2240. [CrossRef]
54. Long, J.; Ivanov, M.S.; Khomchenko, V.A.; Mamontova, E.; Thibaud, J.-M.; Rouquette, J.; Beaudhiun, M.; Granier, D.; Ferreira, R.A.S.; Carlos, L.D.; et al. Room temperature magnetoelectric coupling in a molecular ferroelectric ytterbium(III) complex. *Science* **2020**, *367*, 671–676. [CrossRef]
55. Margeat, O.; Lacroix, P.G.; Costes, J.P.; Donnadieu, B.; Lepetit, C. Synthesis, structures, and physical properties of copper(II)-gadolinium(III) complexes combining ferromagnetic coupling and quadratic nonlinear optical properties. *Inorg. Chem.* **2004**, *43*, 4743–4750. [CrossRef] [PubMed]
56. Hamamatsu, T.; Matsumoto, N.; Re, N.; Mrozinski, J. Chiral ferromagnetic chain of copper(II)-gadolinium(III) complex. *Chem. Lett.* **2009**, *38*, 762–763. [CrossRef]
57. Yamashita, A.; Watanabe, A.; Akine, S.; Nabeshima, T.; Nakano, M.; Yamamura, T.; Kajiwara, T. Wheel-shaped $Er^{III}Zn^{II}_3$ single-molecule magnet: A macrocyclic approach to designing magnetic anisotropy. *Angew. Chem. Int. Ed. Engl.* **2011**, *50*, 4016–4019. [CrossRef] [PubMed]
58. Visinescu, D.; Alexandru, M.-G.; Madalan, A.M.; Pichon, C.; Duhayon, C.; Sutter, J.-P.; Andruh, M. Magneto-structural variety of new 3d-4f-4(5)d heterotrimetallic complexes. *Dalton Trans.* **2015**, *44*, 16713–16727. [CrossRef] [PubMed]
59. Fustero, S.; Román, R.; Asensio, A.; Maesto, M.A.; Aceña, J.L.; Simón-Fuentes, A. An approach to 2,4-substituted pyrazolo[1,5-*a*]pyridines and pyrazolo[1,5-*a*]azepines by ring-closing metathesis. *Eur. J. Org. Chem.* **2013**, 7164–7174. [CrossRef]
60. Sun, J.-W.; Zhu, J.; Song, H.-F.; Li, G.-M.; Yao, X.; Yan, P.-F. Spontaneous resolution of racemic salen-type ligand in the construction of 3d homochiral lanthanide frameworks. *Cryst. Growth Des.* **2014**, *14*, 5356–5360. [CrossRef]
61. Gao, B.; Zhang, Q.; Yan, P.; Hou, G.; Li, G. Crystal engineering of salen type cerium complexes tuned by various cerium counterions. *CrystEngComm* **2013**, *15*, 4167–4175. [CrossRef]